Controls on Dissolved Barium and Radium-226 Distributions in the Pacific Ocean Along GEOTRACES GP15

Emilie Le Roy, Matthew Charette, Paul Henderson, Alan Shiller, Willard Moore, Nathaniel Kemnitz, Douglas Hammond, Tristan Horner

Global Biogeochemical Cycles

RESEARCH ARTICLE
10.1029/2023GB008005

Special Collection:
The U.S. GEOTRACES Pacific Meridional Transect (GP15)

Controls on Dissolved Barium and Radium-226 Distributions in the Pacific Ocean Along GEOTRACES GP15

Emilie Le Roy[1,2], Matthew A. Charette[2], Paul B. Henderson[2], Alan M. Shiller[3], Willard S. Moore[4], Nathaniel Kemnitz[5], Douglas E. Hammond[5], and Tristan J. Horner[2]

[1]Laboratoire des sciences de l'environnement marin - IUEM, Université de Brest - UMR 6539 CNRS/UBO/IRD/Ifremer, Plouzané, France, [2]Department of Marine Chemistry and Geochemistry, Woods Hole Oceanographic Institution, Woods Hole, MA, USA, [3]Stennis Space Center, Institute of Marine Sciences, University of Southern Mississippi, Hattiesburg, MS, USA, [4]School of the Earth, Ocean and Environment, University of South Carolina, Columbia, SC, USA, [5]Department of Earth Sciences, University of Southern California, Los Angeles, CA, USA

Key Points:

- Water mass analysis shows significant shallow deficits and deep excesses of dissolved ^{226}Ra and Ba in the Pacific Ocean along the GP15
- Shallow deficits seem driven by $BaSO_4$ precipitation, deep excesses reflect benthic inputs that are more significant for ^{226}Ra than for Ba
- Budgets suggest that regional barium fluxes nearly balance, and the Pacific is likely a significant source of radium-226 to the global ocean

Correspondence to:
E. Le Roy,
emilie.leroy@univ-brest.fr

Citation:
Le Roy, E., Charette, M. A., Henderson, P. B., Shiller, A. M., Moore, W. S., Kemnitz, N., et al. (2024). Controls on dissolved barium and radium-226 distributions in the Pacific Ocean along GEOTRACES GP15. *Global Biogeochemical Cycles*, *38*, e2023GB008005. https://doi.org/10.1029/2023GB008005

Received 16 OCT 2023
Accepted 21 MAY 2024

Abstract Radium-226(^{226}Ra) and barium (Ba) exhibit similar chemical behaviors and distributions in the marine environment, serving as valuable tracers of water masses, ocean mixing, and productivity. Despite their similar distributions, these elements originate from distinct sources and undergo disparate biogeochemical cycles, which might complicate the use of these tracers. In this study, we investigate these processes by analyzing a full-depth ocean section of ^{226}Ra activities ($T_{1/2}$ = 1,600 years) and barium concentrations obtained from samples collected along the US GEOTRACES GP15 Pacific Meridional Transect during September–November 2018, spanning from Alaska to Tahiti. We find that surface waters possess low levels of ^{226}Ra and Ba due to export of sinking particulates, surpassing inputs from the continental margins. In contrast, deep waters have higher ^{226}Ra activities and Ba concentrations due to inputs from particle regeneration and sedimentary sources, with ^{226}Ra inputs primarily resulting from the decay of ^{230}Th in sediments. Further, dissolved ^{226}Ra and Ba exhibit a strong correlation along the GP15 section. To elucidate the drivers of the correlation, we used a water mass analysis, enabling us to quantify the influence of water mass mixing relative to non-conservative processes. While a significant fraction of each element's distribution can be explained by conservative mixing, a considerable fraction cannot. The balance is driven using non-conservative processes, such as sedimentary, rivers, or hydrothermal inputs, uptake and export by particles, and particle remineralization. Our study demonstrates the utility of ^{226}Ra and Ba as valuable biogeochemical tracers for understanding ocean processes, while shedding light on conservative and myriad non-conservative processes that shape their respective distributions.

1. Introduction

Barium (Ba) and radium (Ra) are alkaline earth elements with similar geochemical behaviors and distributions in the ocean (Chan et al., 1976; Fanning et al., 1988; Mathieu & Wolgemuth, 1973). These similarities led to Ba being proposed as a stable analog of radium-226 (^{226}Ra, t1/2 = 1,600 years; e.g., Broecker et al., 1967). Similar to the $^{14}C/^{12}C$ ratio, the ^{226} Ra/Ba ratio was aimed at being used as a chronometer of the global thermohaline circulation but better tailored to the timescales of ocean circulation. As a result, a unique ^{226}Ra and Ba database was generated during the Geochemical Ocean Sections Study (GEOSECS) program throughout the major ocean basins (Broecker et al., 1970; W. S. Broecker et al., 1967; Chan et al., 1976; Chung & Craig, 1980; Chung et al., 1974; Ku & Lin, 1976; Ku et al., 1970, 1980). However, it was realized that ^{226}Ra and Ba are active participants in upper ocean biogeochemical cycles, which complicated the use of the ^{226}Ra/Ba ratio as a time tracer for deep-water ventilation.

Despite sharing a similar marine distribution, the major sources of radium-226 and barium in seawater are different: ^{226}Ra is sourced mostly by diffusion from deep-sea sediments following the decay of its parent isotope, ^{230}Th (Koczy, 1958; Kröll, 1953), whereas Ba is sourced largely from rivers and groundwater (Martin & Meybeck, 1979; Moore, 1997; Shaw et al., 1998; Wolgemuth & Broecker, 1970). Both ^{226}Ra and Ba have a nutrient-like distribution in the ocean, whereby their concentrations tend to increase with depth, reflecting their removal into particulate phases in shallow waters, and subsequent release at depth, either in the water column or sediments (Broecker et al., 1970; Cochran & Krishnaswami, 1980; Kemnitz et al., 2023; Ku et al., 1980; Ku &

Luo, 1994; McManus et al., 1999). The principal particulate carrier of ^{226}Ra and Ba is thought to be barite ($BaSO_4$ or barium sulfate; Chow & Goldberg, 1960; Dehairs et al., 1980; Bishop, 1988), though contributions from other biominerals are postulated (e.g., celestite; Bernstein & Byrne, 2004). Regardless of the carrier phase, ^{226}Ra and Ba distributions appear to be affected by similar processes in the water column, with both elements displaying a linear correlation throughout the global ocean, except for the deep North Pacific (Chan et al., 1976; Foster et al., 2004; Ku et al., 1980; Le Roy et al., 2018; Li et al., 1973; Östlund et al., 1987).

While the global GEOSECS program provided valuable information on the similarity of the geochemical distributions of ^{226}Ra and Ba in the ocean, several unknowns remain such as the influence of hydrothermal vents (Hsieh et al., 2021; Kipp, Charette, et al., 2018; Neuholz et al., 2020), particle cycling and associated carrier phases (Dehairs et al., 1980; van Beek et al., 2007), and the significance of submarine groundwater discharge (Charette et al., 2001; Kwon et al., 2014; Le Gland et al., 2017; Rahman et al., 2022; Shaw et al., 1998). In this study, we take advantage of the worldwide program GEOTRACES to provide new insights on the factors that control the distribution of ^{226}Ra and Ba in the ocean. Here, we focus on the GEOTRACES GP15 transect in the Pacific Ocean along the 152°W meridian from 56°N to 20°S. This transect allowed us to study a range of processes that influence ^{226}Ra and Ba distributions, including margin fluxes, low productivity surface waters, as well as hydrothermal plumes of the East Pacific Rise. The North Pacific is recognized as harboring the most ancient deep water found in the world's oceans, as defined by $^{14}C/^{12}C$ (Matsumoto, 2007). Moreover, it is thought that upwelled Pacific waters act as the primary source of upper ocean winter waters departing the Southern Ocean in the form of Subantarctic Mode Water, supplying nutrients to the ocean's upper thermocline, which are crucial to the biological productivity (e.g., Sarmiento et al., 2004; Talley, 2013). Consequently, the factors controlling ^{226}Ra and Ba in the Pacific Ocean will have an outsized impact on the distribution of these tracers throughout the global thermohaline circulation, making the GP15 section an ideal transect for studying these processes.

2. Materials and Methods

The US GEOTRACES GP15 Pacific Meridional Transect was conducted in the Pacific Ocean primarily along 152°W from 56°N to 20°S (Figure 1). The R/V *Roger Revelle* departed Seattle (Washington) in September 2018, sailed northwest to the Alaskan Shelf, and then turned eastward across the shelf before heading southward. After a stop in Hilo (Hawaii, US), it reached Papeete (Tahiti, French Polynesia) on 24 November 2018. Along the transect, 39 stations were sampled, with full-water column ^{226}Ra and Ba sampling taking place at alternating stations. Radium-228 data from GP15 have been published separately (Moore et al., 2024).

2.1. Hydrographic Context

2.1.1. Surface and Subsurface Water Masses

On the surface of the North Pacific around 50° N, the Subarctic Current flows eastward as the Pacific Subarctic Water (PSUW), which is characterized by relatively high oxygen and low temperature and salinity (Sverdrup et al., 1942; Talley et al., 2011b). Then, Pacific Subarctic Water splits into two branches. One branch flows northward as the Alaskan current, while another branch flows southward as the Californian current and mixes with Central Waters (Bograd et al., 2019). Further south and to the east, Eastern North Pacific Central Water (ENPCW) is found between 40°N and the North Equatorial Countercurrent. The Eastern North Pacific Central Water comes from the subduction of a salinity maximum just south of 30°N, including some mixing with Pacific Subarctic Water (Tomczak & Liefrink, 2005). Similarly, the South Pacific Central Water (SPCW) extends from the subantarctic front at 55° S to 10° S. SPCW is saltier than Eastern North Pacific Central Water since the South Pacific is saltier overall. Equatorial Subsurface Water (ESSW) is formed near the equator, as a mixture of several water masses, and is characterized by its relatively high salinity (Silva et al., 2009). Equatorial Subsurface Water is transported eastward to the South American coast along the equator within the Equatorial Undercurrent and Southern Subsurface counter currents (Montes et al., 2014; Stramma et al., 2010), and then southward along the South American coast within the Peru-Chile countercurrent (Strub et al., 1998).

2.1.2. Intermediate Water Masses

The intermediate layer of the Pacific Ocean is occupied by Antarctic Intermediate Water (AAIW) and North Pacific Intermediate Water (NPIW). Both Antarctic Intermediate Water and North Pacific Intermediate Water are fresh and cool surface waters that subduct at subpolar latitudes. Antarctic Intermediate Water is formed by

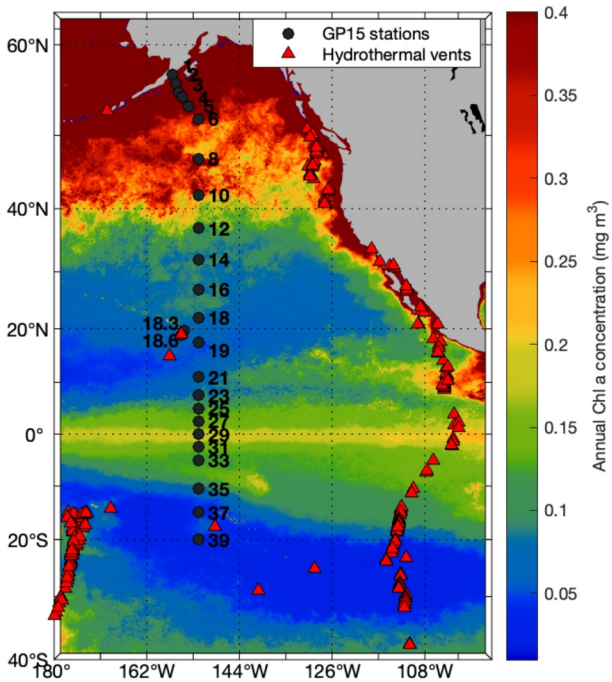

Figure 1. Map of time-averaged chlorophyll a concentration (mg m^{-3}) for 2018 (yearly 4 km MODIS Aqua model). Station locations of the GP15 section between Alaska and Tahiti in the Pacific (black dots). The known hydrothermal vents located in the Pacific are indicated (red triangles; Beaulieu & Szafranski, 2020).

subduction of surface waters beneath the Subantarctic Front near the west coast of Chile, flowing north and then west within the gyre circulation (Tomczak & Liefrink, 2005). Antarctic Intermediate Water is characterized by a subsurface salinity minimum, high O_2, and low nutrients (Hartin et al., 2011; Iudicone et al., 2007; Talley et al., 2011a). North Pacific Intermediate Water is formed from ventilated water in the Sea of Okhotsk and the adjacent polar gyre, and is also characterized by a salinity minimum (Talley, 1997). It is confined to the North Pacific.

2.1.3. Deep and Bottom Water Masses

Pacific Deep Water (PDW) has no surface source and as a result is consider one of the oldest water masses in the global ocean (Talley et al., 2011a). Pacific Deep Water is formed in the deep waters of the equatorial Pacific through upwelling and diapycnal diffusion of northward-flowing bottom waters. Pacific Deep Water has relatively low O_2, and high nutrients, and is often characterized by a broad $Si(OH)_4$ maximum (Faure & Speer, 2012; Hautala, 2018; Hautala & Hammond, 2020; Johnson & Toole, 1993; Mantyla & Reid, 1983; Tsuchiya & Talley, 1998; Wijffels et al., 2001). Lower Circumpolar Deep Water (LCDW) and Upper Circumpolar Deep Water (UCDW) lie below Pacific Deep Water and originate in the Southern Ocean. Circumpolar Deep Waters are a mixture of Pacific, Atlantic, and Indian Ocean waters modified by the incorporation of dense water produced around the Antarctica continent. Lower Circumpolar Deep Water properties change while flowing northward as the layer erodes and upwells across isopycnals. Indeed, LCDW salinity decreases northward and is the lowest near the Hawaii ridge. Upper Circumpolar Deep Water is identified with an O_2 minimum (Orsi et al., 1999; Talley et al., 2011a; Tomczak & Liefrink, 2005), as it is formed from modified Pacific Deep Water and is influenced by Indian Deep Water and the upwelling of relatively lower-nutrient Lower Circumpolar Deep Water and North Atlantic Deep Water from below (Talley et al., 2011a). Upper Circumpolar Deep Water flows into the Pacific Basin at a similar isopycnal range as Pacific Deep Water. Antarctic Bottom Water (AABW) is formed through brine rejection along the shelves of the Antarctic continent, where these newly formed highly saline shelf waters sink to abyssal depths. Antarctic Bottom Water is characterized by a potential temperature minimum and occupies the deepest waters in the low-latitude Pacific.

2.2. Sample Collection

Dissolved ^{226}Ra samples were collected in 30 L Niskin bottles. For deep casts (>1,000 m), these bottles were mounted directly above the large-volume in situ WTS-LV pumps (McLane Labs), whereas for casts <1,000 m bottles were mounted on a CTD rosette. Between 10 and 25 L from each bottle was gravity filtered at ~0.5 L min^{-1} through 15 g of manganese oxide-impregnated acrylic fiber (Mn Fiber), which quantitatively adsorbs radium isotopes (assumed to scavenge 100% of Ra; van Beek et al., 2010; Moore, 1976). The filtrate was collected inside a graduated rigid-sided container and the volume was recorded. Mass was also obtained by weighing with a hanging digital balance.

Samples for dissolved Ba were collected using a GEOTRACES CTD referred to as GT-C/12 L GoFlo. Water samples were filtered through pre-cleaned, 0.2 μm Pall Acropak Supor filter capsules (GEOTRACES Standards and Intercalibration Committee, 2017; Hatta et al., 2014). Filtered water was collected in 125 mL HDPE bottles (Nalgene) that had been pre-cleaned by soaking in 1.2 M HCl (reagent grade) for at least 8 hr, with a subsequent thorough rinsing using ultrapure distilled deionized water (Barnstead E-pure).

2.3. Sample Analysis

2.3.1. Analysis of Dissolved ^{226}Ra Concentrations

Radium-226 activities were measured using the radon emanation method, which enables the measurement of ^{226}Ra via its daughter, radon-222 (^{222}Rn; half-life of 3.8 days). Mn Fiber samples were flushed with helium for

5 min at 250 mL min^{-1} into PVC cartridges (Peterson et al., 2009). The cartridges were sealed and held for a minimum of 5 days and up to 2 weeks. Before analyses, the radon emanation line was purged with helium for 10 min. The helium flow was then diverted through the cartridge containing the sample for 15 min to flush the ingrown ^{222}Rn into a liquid nitrogen trap. Then, the cartridge was again bypassed and the liquid nitrogen trap was heated so that ^{222}Rn was transferred to an evacuated "Lucas cell" via a stream of helium (Key et al., 1979; Lucas, 1957; Peterson et al., 2009). The cells were held for 3 hr to reach the secular equilibrium among the ^{222}Rn decay chain daughters and then placed on a radon counting system (model AC/DC-DRC-MK 10-2) for 1–20 hr to reach counting uncertainties (1 SD) of 2%–5%.

The method was standardized using National Institute of Standards and Technology ^{226}Ra (~20 dpm) sorbed onto Mn fiber and analyzed in the same manner as the samples (Charette et al., 2015; Henderson et al., 2013). Backgrounds of the radon scintillation cells were counted for 10 min before each sample analysis and can represent up to 7% of the total measured activity. The final sample measurement error was based on the counting uncertainty, the standard deviation of the Lucas cell background, and the standard deviation of the detector efficiency. The errors ranged mostly between 2% and 6%. While replicates were not collected for ^{226}Ra due to sample volume limitations, for some stations, overlapping depths between CTD casts were occasionally sampled with generally good agreement. Any small discrepancies between the two casts may be due to the drift of the boat between casts or slight changes in sampling depth. As another check on data quality, station 35 from GP15 was a reoccupation of station 36 from GP16 (2013) with the ^{226}Ra profile between cruises showing relatively good agreement. Since ^{226}Ra is known to have a linear relationship with barium and silicate for shallow and intermediate depths, any samples exhibiting values beyond two standard deviations of the expected values were remeasured. If the reanalysis confirmed the original value, then the samples were flagged (27 samples out of 415) as suspect and excluded from figures or analyses.

2.3.2. Analysis of Dissolved Ba Concentrations

Dissolved Ba concentrations were determined using isotope dilution, measured on a ThermoFisher Element XR Inductively Coupled Plasma Mass Spectrometer (ICPMS; e.g., Jacquet et al., 2005). A 50 µL aliquot of each sample was spiked with 25 µL of a 93% ^{135} Ba-enriched solution (Oak Ridge National Laboratories; ~170 nM) and then diluted 30-fold with 0.2 µm ultrapure filtered water. For quality control purposes, the spike calibration was checked twice during each analytical run using reverse isotope dilution. The ICP-MS was operated in low resolution and both ^{135}Ba and ^{138}Ba were determined. The samples were bracketed every 10 samples with a blank and the ^{135}Ba-spike solution. The volumes of the spikes, samples, and dilution water were accurately assessed by calibrating each pipette by weight. The reproducibility error of this method was estimated by comparing samples collected at the same depths on different casts at the same station. For 12 pairs of these replicate samples, the average absolute deviation was 0.7 nmol kg^{-1} or ~1.5%. Repeated runs of US GEOTRACES intercalibration samples and in-house reference solutions suggest a similar precision (Shiller, 2021a, 2021b, 2021c). The limit of detection for barium was 0.7 nmol L^{-1}. Our precision is similar to that reported by other labs for Ba (e.g., Jacquet et al., 2005). As for ^{226}Ra, station 35 from GP15 was a reoccupation of station 36 from GP16 (2013) with the Ba profile between cruises showing good agreement (Rahman et al., 2022).

2.3.3. Water Mass Decomposition

Water mass fractions are useful in understanding trace element and isotope distributions along a transect. A modified version of an Optimum Multiparameter Analysis (Shrikumar et al., 2022) was employed to determine water mass fractions in GP15 samples (Lawrence et al., 2022). Then, based on historical data reported from the Pacific (Chan et al., 1976, 1977; Ku et al., 1980), we defined ^{226}Ra and Ba end member concentrations associated with each water mass (Figure 2). The characteristics of each water mass (potential temperature, salinity, and geographical location) were used to determine the end members of ^{226}Ra and Ba. The end members are all in the range of the GP15 data (Figure 2). These ^{226}Ra and Ba end members were then used to calculate the ^{226}Ra and Ba concentrations that strictly result from the mixing of the different water masses. In this way, we estimated the conservative component of ^{226}Ra and Ba, which can in turn be compared to the in situ concentrations to generate the non-conservative components of ^{226}Ra and Ba (hereafter referred to as anomalies) along the GP15 section.

To incorporate uncertainties associated with the end-member compositions into the water mass analysis, we employed a Monte Carlo approach, generating 10,000 random perturbations of each water mass end-member.

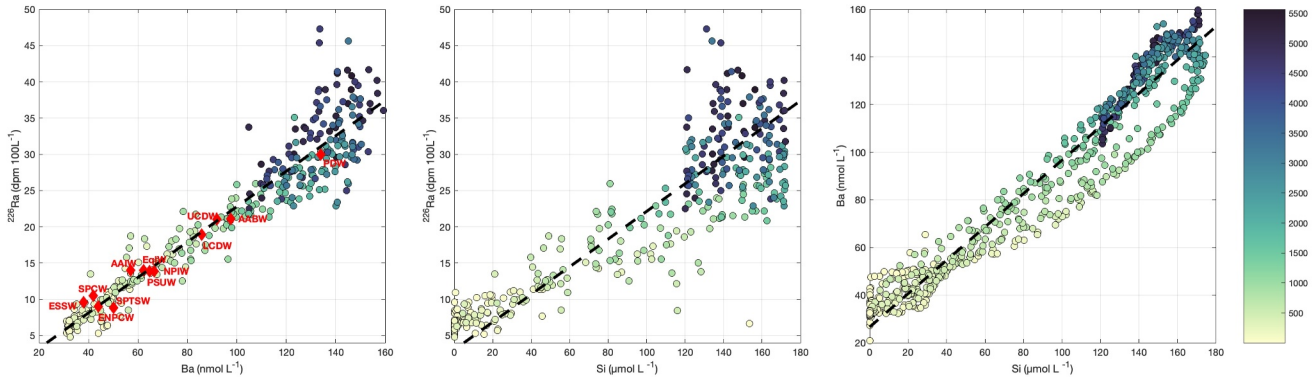

Figure 2. Relationships between ^{226}Ra and Ba, ^{226}Ra and Si, and Ba and Si along the GP15 section. The color scale represents the depth of each sample. The best linear fits for ^{226}Ra and Ba ($R^2 = 0.89$, $P < 0.0001$), ^{226}Ra and Si ($R^2 = 0.81$, $P < 0.0001$), and Ba and Si ($R^2 = 0.94$, $P < 0.0001$) are also reported (dashed black lines). The slopes of the ^{226} Ra-Ba, ^{226}Ra-Si, and Ba-Si linear regressions are 2.36 ± 0.04 dpm μmol^{-1}, 52.42 ± 1.26 dpm mmol^{-1} and 1,428.1 ± 12.2, respectively. Water mass end members are also reported for ^{226}Ra-Ba (red diamonds).

This analysis resulted in estimated conservative component uncertainties of ±0.9 dpm 100 L^{-1} for ^{226}Ra and ±4.0 nmol L^{-1} for Ba. Subsequently, when the measured ^{226}Ra or Ba values differed from the conservative component values, and these differences exceeded their respective analytical uncertainties, the ^{226}Ra or Ba anomalies were deemed non-conservative. Non-conservative values could manifest as either positive (indicative of a net addition of ^{226}Ra or Ba) or negative (reflective of a net removal of ^{226}Ra or Ba).

We compared the water mass analysis-derived Ra and Ba anomalies to Ra* and Ba* to validate the use of water mass deconvolution (Figure 3). First defined by Horner et al. (2015) for the global Ocean, Ba* is the difference between measured and predicted [Ba] based on the Ba–Si linear regression (Figure 2). Similarly, Ra* is the difference between measured and predicted ^{226}Ra based on the ^{226}Ra–Si linear regression (Figure 2).

$$Ba^* = Ba_{\text{in situ}} - 0.66 \times Si_{\text{in situ}} - 29.6 \quad (1)$$

$$Ra^* = Ra_{\text{in situ}} - 0.15 \times Si_{\text{in situ}} - 6.1 \quad (2)$$

The distribution of Ra* and Ba* can be interpreted as vertical or spatial differences in Ba and Si sources or sinks, with the net effects defining the direction and magnitude of the deviation (Mete et al., 2023). $BaSO_4$ precipitation and SiO_2 dissolution produce more negative Ba* and with $BaSO_4$ dissolution and SiO_2 precipitation produce

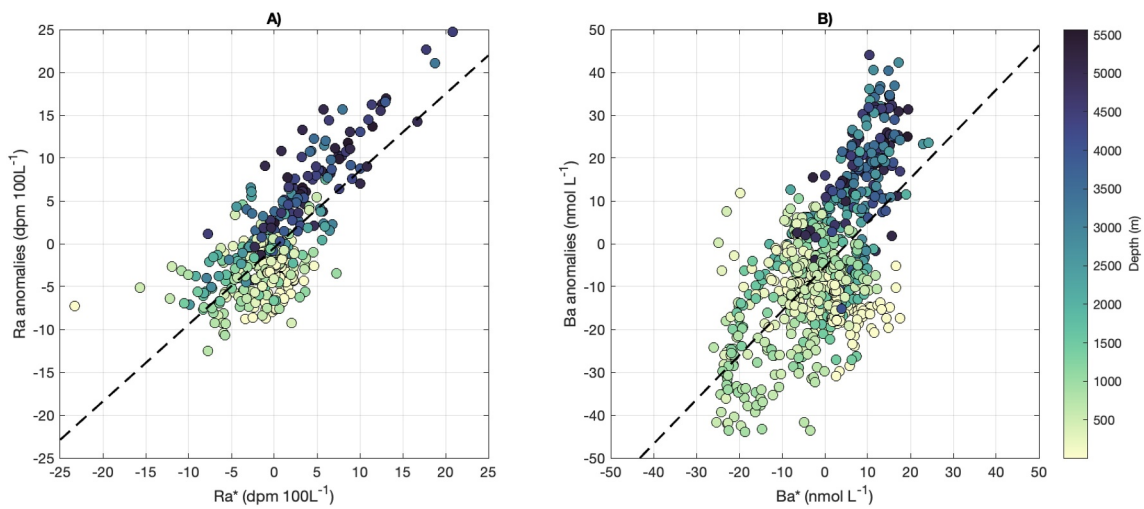

Figure 3. Relationships between Ba* and Ba anomalies along the GP15 section. The color scale represents the depth of each sample. Ba* is calculated from a regression versus Si. The best linear fit ($R^2 = 0.65$, $P < 0.0001$) is also reported (dashed black line). The slope of the Ba* and Ba anomaly relationship is 1.08 ± 0.03.

more positive Ba* relative to mean-ocean behavior (Mete et al., 2023). A comparison of Ra* and Ba* and Ra and Ba anomalies derived using the OMP yields a linear slope of 0.89 ± 0.04 ($R^2 = 0.52$, $p < 0.0001$) and 1.04 ± 0.05 ($R^2 = 0.36$, $p < 0.0001$), respectively (Figure 3). The scatter likely reflects the fact that different water masses possess distinct preformed Ra* and Ba* and that the magnitudes of $BaSO_4$ precipitation/dissolution and SiO_2 precipitation/dissolution may differ regionally.

3. Results

3.1. Distribution of ^{226}Ra and Ba Along the GP15 Section

The ^{226}Ra, Ba, and ^{226}Ra/Ba ratio distributions for the GP15 section are presented in Figure 4. Most of the ^{226}Ra activities range from 4 to 40 dpm 100 L^{-1} in the water column, with an increase toward the bottom. Higher activities are observed between the equator and 45°N below 2,000 m. Barium concentrations increase with depth from 30 to 160 nmol L^{-1}. Below 1,500 m, Ba concentrations increase from south to north from 120 nmol L^{-1} at 20°S to 150 nmol L^{-1} at 50°N. These data are in agreement with data from Pacific GEOSECS and GEOTRACES GP16 crossover stations, which range from 5 to 45 dpm 100 L^{-1} (Sanial et al., 2017) and from 20 to 156 nmol L^{-1} for Ba (Rahman et al., 2022).

3.2. ^{226}Ra Versus Ba Relationship

The ^{226}Ra/Ba ratio varies from 1.5 to 4.8 along the GP15 section (Figure 4c). The average ratio of 2.2 dpm μmol^{-1} is also consistent with the historical data (Broecker et al., 1970; Chan et al., 1976; Chung & Craig, 1980; Ku et al., 1980; Le Roy et al., 2018). Higher-than-average ^{226}Ra/Ba ratios are observed between the equator and 40°N below 3,000 m, and to a lesser extent between 15°S and 15°N at 500 m to and 2,500 m. Low ratios (<2.2 dpm nmol^{-1}) are generally confined to the upper 200 m, though some low ^{226}Ra/Ba ratios are observed north of 30° N at 1,500 m and 4,000 m.

A linear correlation between ^{226}Ra and Ba is observed for the data collected along the GP15 section (Figure 2). The slope of the ^{226}Ra-Ba linear regression is 2.36 ± 0.04 dpm μmol^{-1} ($R^2 = 0.89$, $P < 0.0001$; Figure 2). As previously observed, the relationship breaks down for ^{226}Ra values > 30 dpm 100 L^{-1} (Chan et al., 1976; Chung & Craig, 1980). The GP15 linear regression intercept for Ba is +6.7 nmol L^{-1}. Positive intercepts have been previously observed in the Atlantic and have been attributed to larger terrestrial Ba inputs relative to ^{226}Ra (Ku & Luo, 1994; Le Roy et al., 2018). Alternatively, this intercept may signify less efficient removal of Ba relative to ^{226}Ra by the biological pump (see Section 4.2.1).

3.3. Distribution of ^{226}Ra, Ba, and ^{226}Ra/Ba Anomalies

Our analysis reveals that half of the ^{226}Ra data are considered non-conservative along the section (Figure 5a). Most of the positive anomalies are observed below 3,000 m, with the highest anomalies located between the equator and 40°N. The negative anomalies occur mostly in the upper 2,000 m. From 20°N to the Alaskan margin, in the first 1,500 m, the average anomaly is −2.8 dpm 100 L^{-1}.

Negative ^{226}Ra anomalies are mostly observed between 200 and 1,000 m, while positive Ba anomalies are mostly observed below 2,000 m (Figure 5b). The most geographically extensive negative anomalies are observed from the surface to 1,500 m, north of 20°N, with an average negative anomaly of −8.9 nmol L^{-1}.

For 35% of the samples, the ^{226}Ra/Ba anomaly ratio does not show significant variations (Figure 5c). Positive ^{226}Ra/Ba anomalies are mostly displayed below 3,000 m. Other positive anomalies are observed around 2,500 m, from 20°S to 5°N, with an average of +0.13 dpm μmol^{-1}. Some positive anomalies are observed between 5°S and 5°N in the first 2,000 m. Negative ^{226}Ra/Ba anomalies, found in 36% of the samples, are found in multiple locations along the section: between 500 and 1,500 m in the southernmost part of the section, in the first 500 m from 5°S to 15°N, and from 1,000 m at 15°N and deeper moving north toward the Alaskan margin.

4. Discussion

Here, we examine the non-conservative component of the distribution of ^{226}Ra and Ba along GP15 and outline the processes that sustain it. We then discuss the sinks and sources of the two elements, and construct budgets of ^{226}Ra and Ba for the Pacific Ocean. To simplify this latter calculation, we considered the Pacific

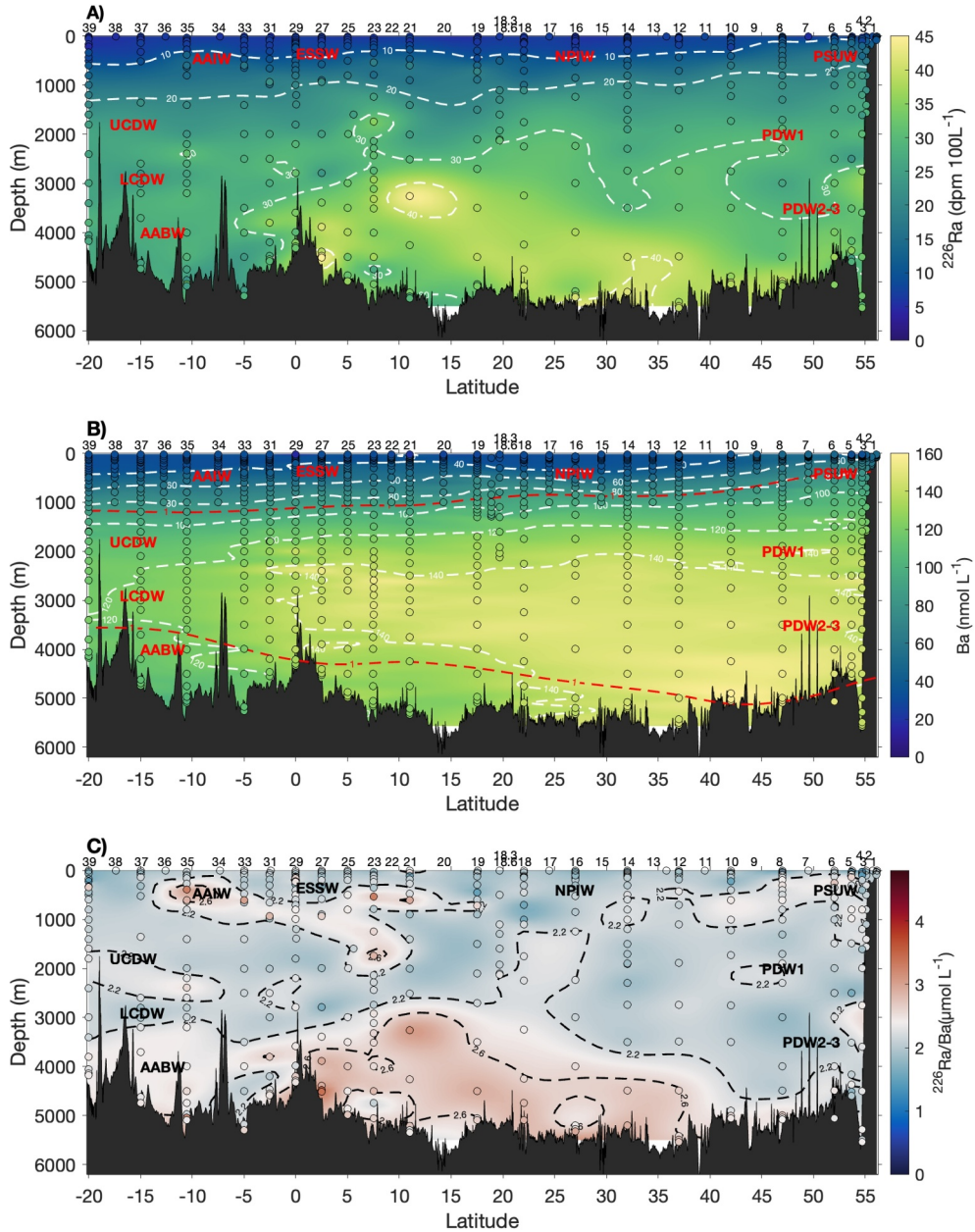

Figure 4. (a) Distribution of dissolved ^{226}Ra activities (dpm 100 L^{-1}), (b) dissolved Ba concentrations (nmol L^{-1}), and (c) dissolved ^{226}Ra/Ba ratios along the GP15 section. Station numbers are found on the top of the panel. The sampling depths are shown for each vertical profile (dots). The different water masses are also reported: ESSW: Equatorial Subsurface Water, NPIW: North Pacific Deep Water, PDW: Pacific Deep Water, PSUW: Pacific Subarctic Water, LCDW: Lower Circumpolar Deep Water, UCDW: Circumpolar upper Deep Water, AABW: Antarctic Bottom Water.

Ocean in terms of two boxes—a surface box that extends to 1,000 m, and a deep box from 1,000 m to the seafloor. The 1,000 m boundary was justified by two factors. First, surface and intermediate water masses are predominantly found above 1,000 m, whereas deep water masses are typically found below this depth. Second, this designation ensures that the mesopelagic zone, defined as between 200 and 1,000 m, is encompassed entirely by the upper box. We used an average depth of 4,280 m and an area of 1.62×10^{14} m^2 for the Pacific (Costello et al., 2015) This division helps simplify the calculation of ^{226}Ra and Ba sinks and sources, which sometimes operate in only a single box.

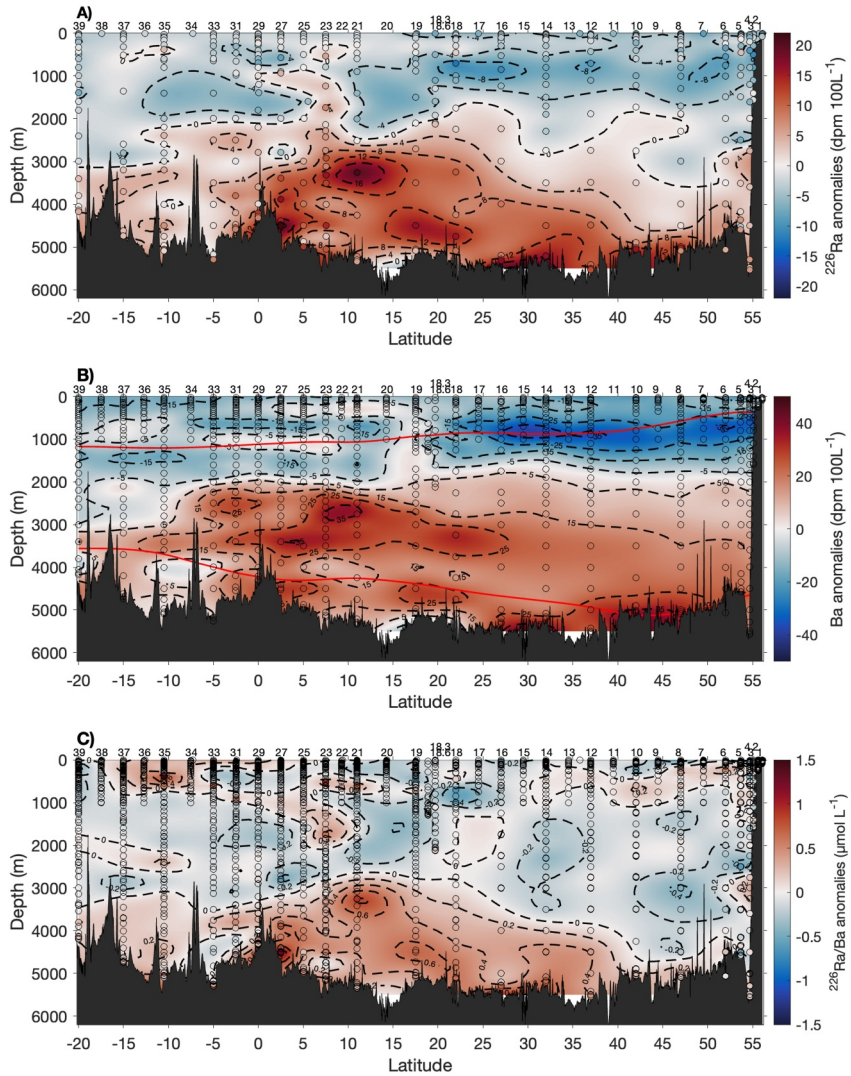

Figure 5. Distribution of (a) dissolved ^{226}Ra activity anomalies (dpm 100 L^{-1}) and (b) dissolved Ba concentration anomalies (nmol L^{-1}) with the barite saturation index (red contour lines), and (c) dissolved ^{226}Ra/Ba anomalies along the GP15 section. Station numbers are found on top of each panel.

4.1. The Behavior of ^{226}Ra and Ba Along GP15

4.1.1. Role of Physical Circulation

In the deep Pacific, the activities of ^{226}Ra and concentrations of Ba ([Ba]) are among the highest observed in the global ocean. These elevated values, reaching 45 dpm 100 L^{-1} and 160 nM, reflect a combination of both in situ processes and physical circulation. In considering the magnitude of these anomalies, it is helpful to first consider the starting point for Pacific Deep Water. While Antartic Bottom Water flows down the shelf of Antarctica to abyssal depths in the Pacific, it becomes enriched in ^{226}Ra and Ba as it contacts the sediments, resulting in end-member Antartic Bottom Water ^{226}Ra activities and [Ba] of ≈20 dpm 100 L^{-1} and ≈100 nM, respectively (e.g., Chung, 1980; Hoppema et al., 2010). Then, Lower Circumpolar Deep Water and Upper Circumpolar Deep Water carry that initial enrichment along their flow path northward. Pacific Deep Water is formed in the deep waters in the equatorial Pacific through upwelling and diapycnal diffusion of Lower Circumpolar Deep Water and Upper Circumpolar Deep Water. Thus, Pacific Deep Water starts with high initial ^{226}Ra activities and Ba concentrations though this only explains some of the observations.

The significant benthic anomalies of ^{226}Ra and Ba between the Equator and 40°N are likely the result of a recirculating water parcel originating around ∼40°N and ∼170°W. These waters spiral cyclonically at the bottom for an estimated 685 years while moving slowly upward by ≈1,000 m and advecting eastward, intersecting the GP15 section (152°W) around 40°N (Hautala, 2018). Upward diapycnal velocities reach maximum values between 20°N and 40°N in the North Pacific (Arzel & Verdière, 2016). This recirculation allows deep waters to accumulate ^{226}Ra and Ba from the seafloor. This accumulation is consistent with the higher copper and neodymium concentrations (Bian et al., 2022a, 2022b; Shiller, 2021b, 2021c) and the high benthic Ba and ^{228}Ra fluxes reported in this region (Moore et al., 2024; Steiner et al., 2023).

4.1.2. Non-Conservative Anomalies

Our water mass analysis indicates that a portion of the ^{226}Ra and Ba can be explained by conservative mixing of different water masses. The remainder must reflect other processes, the nature of which can be inferred from the location, extent, and intensity of the non-conservative anomalies. For example, one of the most striking features of the dissolved ^{226}Ra and Ba distributions along GP15 are the large negative anomalies close to the Alaskan Margin, particularly large for Ba (Stations 1–8; Figures 5a and 5b). These anomalies are greatest near the surface but extend to around 1,000 m for Ba and as deep as 3,000 m for ^{226}Ra. The origin of these anomalies is related to the transfer of dissolved ^{226}Ra and Ba from the dissolved phase to particles, with a stronger removal of Ba relative to ^{226}Ra. The mechanism of removal likely relates to pelagic $BaSO_4$ precipitation, which is thought to occur in the upper mesopelagic realm (e.g., Light & Norris, 2021; Stroobants et al., 1991). The negative anomalies in ^{226}Ra and Ba extend into the bathypelagic region implies that considerable $BaSO_4$ formation occurred in these waters between their surface source region and the GP15 section, substantial deep $BaSO_4$ precipitation in the North Pacific (e.g., van Beek et al., 2007; van Beek et al., 2022), or a combination of both processes.

In contrast to the upper 1,000 m, almost the entire deep GP15 section is characterized by positive ^{226}Ra and Ba anomalies. These anomalies exhibit distinct vertical and spatial patterns along the section. Broadly, these anomalies are thought to represent four distinct processes discussed in detail in Section 4.3: remineralization of surface-derived particles containing ^{226}Ra and Ba (Section 4.3.1); intermediate-depth anomalies for ^{226}Ra but not Ba south of the equator, possibly originating from hydrothermal sources (Section 4.3.3); significant excesses in ^{226}Ra and Ba within the bottom 2,000 m, particularly between the equator and 40°N (Section 4.3.4); and, a ^{226}Ra/Ba deficit in the far North Pacific below 3,000 m, which may be explained by the radioactive decay of ^{226}Ra (Section 4.2.3).

4.2. Sinks of ^{226}Ra and Ba

4.2.1. Barite Precipitation

The principal dissolved–particulate transformation affecting dissolved Ba in seawater is the formation of microcrystalline $BaSO_4$, which is also the principal host phase of particulate Ba in suspended particulate matter (e.g., Bishop, 1988; Dehairs et al., 1980; Dickens et al., 2003; Griffith & Paytan, 2012; Horner & Crockford, 2021, 2021; Jacquet et al., 2007; Paytan & Kastner, 1996). However, in undersaturated waters, barite precipitation is not thermodynamically favored, and therefore, barite formation is likely mediated via biological processes (Bertram & Cowen, 1997; Dymond et al., 1992; Martinez-Ruiz et al., 2019). Indeed, bacteria, diatoms, and acantharians (protozoan zooplankton) have all been proposed as mediators of pelagic barite formation (Bishop, 1988; González-Muñoz et al., 2003; Gonzalez-Muñoz et al., 2012). While the exact mechanism of barite formation is still debated, several studies now support the idea that decaying organic matter provides a source of barium and sulfate ions to transient microenvironments that become conducive to barite precipitation before disaggregating (Bishop, 1988; Chow & Goldberg, 1960; Dehairs et al., 1980; Ganeshram & Francois, 2003; Stroobants et al., 1991). This microenvironment model is appealing because it can explain widespread pelagic barite precipitation regardless of the type of organisms present (e.g., Ganeshram et al., 2003). Moreover, the microenvironment model is consistent with the close association between biological productivity and pelagic barite abundance (e.g., Dehairs et al., 1992; Horner et al., 2017; Martinez-Ruiz et al., 2019). Regardless of the formation mechanism, barite crystals are generally viewed as the most important Ba and Ra carriers in the water column (Dehairs et al., 1980, 1990; Legeleux & Reyss, 1996; Moore & Dymond, 1991; Stroobants et al., 1991; van Beek et al., 2007, 2022).

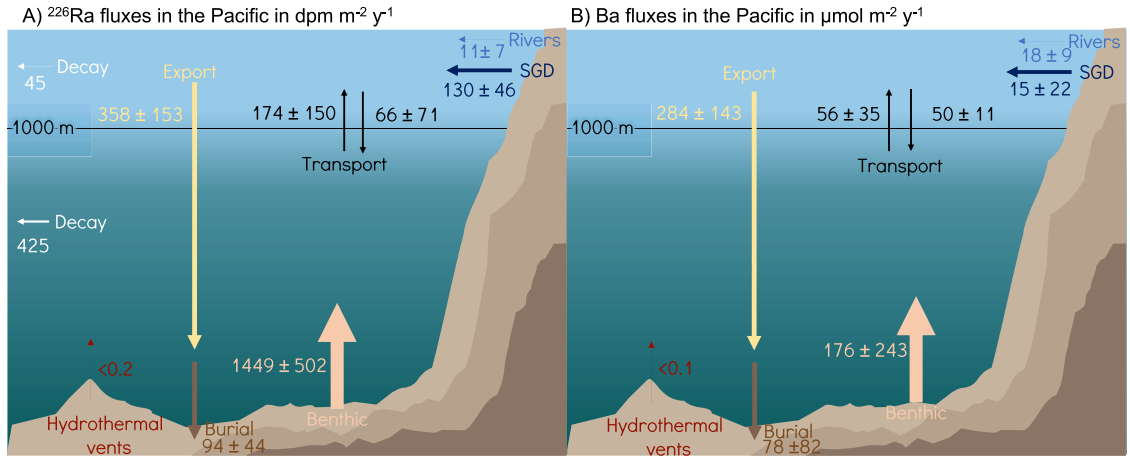

Figure 6. A simplified diagram of the ^{226}Ra and (b) Ba cycles in the Pacific. The flux directions are shown with arrows, with the value of the flux in parentheses (in dpm m^{-2} y^{-1} and µmol m^{-2} y^{-1}).

While the Ba content of organic matter is generally too low to account for widespread surface surface-water Ba depletion, the cycling of organic matter can nonetheless influence the distributions of Ba and ^{226}Ra through the formation of barite (e.g., Horner et al., 2017; Sternberg et al., 2005). Specifically, the northeastern North Pacific is a highly productive area, as evidenced by elevated chlorophyll a (chl a) concentrations from satellite imagery (Figure 1). Near the Alaskan margin (stations 1–8), chl concentrations above 0.4 mg m^{-3} are observed with a sharp decrease southward. $BaSO_4$ formation is generally correlated with organic matter decomposition in the upper mesopelagic zone. Consequently, high productivity in the North Pacific could explain the negative sub-surface Ba and ^{226}Ra anomalies near the Alaskan margin. Moreover, high apparent oxygen utilization (AOU) values (>300 µmol kg^{-1}) are observed at the same location as the Ba negative anomalies. This is consistent with the previously observed correlation between mesopelagic particulate barium concentrations and O_2 consumption rate (Dehairs et al., 1997; Jacquet et al., 2005, 2021), and that AOU generally increases with advancing growth season (Dehairs, 1997; Jochem et al., 1995; Rommets et al., 1997).

It is also possible that the uptake of Ba and ^{226}Ra in the upper water column can be enhanced by substitution of these elements for calcium in calcareous skeletons (Lea & Boyle, 1989, 1990), substitution for Sr in celestite skeletons produced by acantharians (Bernstein et al., 1987, 1992; Jacquet et al., 2007), and potentially by adsorption to diatom frustules (Bishop, 1988; Ganeshram & Francois, 2003; Sternberg et al., 2005; Xu et al., 2022). Indeed, ^{226}Ra has been identified in both zooplankton and phytoplankton (Cherry, 1964; Ku & Lin, 1976; Shannon & Cherry, 1971; Szabo, 1967), with diatoms showing the highest radium content among these organisms.

4.2.2. Particle Burial

A fraction of the ^{226}Ra and Ba removed into particulate $BaSO_4$ is ultimately buried on the seafloor, while the remainder is returned to seawater (discussed in Section 4.3.1.). Since there are currently no satisfactory estimates of particulate ^{226}Ra burial in the Pacific, we estimate this term from Ba. Barium burial is estimated to be -78 ± 82 µmol m^{-2} y^{-1} (Hayes et al., 2021). The average ^{226}Ra/Ba ratios in particles close to the bottom are 1.46 dpm $µmol^{-1}$ (van Beek et al., 2007, 2022). Moore and Dymond (1991) reported a range of 0.8–1.6 dpm $µmol^{-1}$ for ^{226}Ra/Ba in sediment traps deployed near the seabed. These ^{226}Ra/Ba ratios in particles are about half that in the dissolved phase, explained by a discrimination against Ra during crystallization or a preferred dissolution or desorption of Ra over Ba as particles age (van Beek et al., 2007). Applying these ^{226}Ra/Ba ratios to the Ba burial flux allows us to estimate a ^{226}Ra burial flux by barite of -94 ± 44 dpm m^{-2} y^{-1} (Figure 6).

4.2.3. Radioactive Decay

Given that the half-life of ^{226}Ra is similar to the ocean mixing time (both ≈1,000 years), some ^{226}Ra is lost via radioactive decay. Barium is not subject to this loss term. We estimate decay losses of ^{226}Ra for both the surface and deep boxes, which can be calculated using:

$$F_{\text{decay}} = \lambda \times [\text{Ra}] \times h \quad (3)$$

where h is 1,000 m for the surface box (0–1,000 m) and 3,280 m for the deep box (1,000 to 4,280 m). On average in the Pacific, ^{226}Ra in the first 1,000 m is 10.3 and 30 dpm 100 L^{-1} in the deep Pacific. The decay represents a sink of 45 dpm m^{-2} y^{-1} in surface waters and 425 dpm m^{-2} y^{-1} for the deep Pacific (Table 1; Figure 6).

4.3. Sources of ^{226}Ra and Ba

4.3.1. Particle Regeneration

Upper ocean-derived barite has been shown to dissolve at depth in the water column in different ocean basins (Dehairs et al., 1980). The top 1,000 m of the ocean is largely undersaturated with respect to $BaSO_4$, which is where most pelagic $BaSO_4$ is thought to form (Mete et al., 2023; Monnin et al., 1999; Rushdi et al., 2000). However, in the intermediate and deep Pacific, particularly in the north of the basin, there is a slight oversaturation with respect to barite. It is worth noting that the $BaSO_4$ solubility data were derived from experiments using lab-made, coarse-grained $BaSO_4$, which may not accurately represent the microcrystalline $BaSO_4$ precipitates found in seawater (Mete et al., 2023). Assuming that $BaSO_4$ dissolution is related to the degree of undersaturation, dissolution should be greatest near the seafloor and should increase from north to south. Given the nature of this ^{226}Ra and Ba source, and the type of analysis used here, it is difficult to distinguish in situ dissolution from benthic sources, such as diffusion from pore water.

4.3.2. Terrestrial

The variability of ^{226}Ra and Ba concentrations in surface ocean water is small except in coastal regions, where values may increase significantly due to inputs from various sources. These inputs include desorption of ^{226}Ra and Ba from sediment delivered by rivers (Li & Chan, 1979) and submarine groundwater discharge (SGD; Moore, 1996; Shaw et al., 1998). Bullock et al. (2022) estimated (dissolved plus desorbed) ^{226}Ra riverine inputs to the Pacific of (+17.5 ± 11.6) 10^{14} dpm y^{-1}. Scaling this to the surface area of the Pacific yields 10 ± 7 dpm m^{-2} y^{-1}. Bullock et al. (2022) also estimated total SGD inputs to the Global Ocean of 37–57 × 10^{15} dpm y^{-1}. If we assume the SGD inputs are distributed evenly, we can use the fraction of the Global Ocean covered by the Pacific (46%) and the surface area of the Pacific to estimate SGD to the Pacific of +130 ± 46 dpm m^{-2} y^{-1} (Figure 6). Thus, SGD inputs of ^{226}Ra are much more important than riverine inputs to the Pacific, which is consistent with the Pacific ^{228}Ra terrestrial sources (Kwon et al., 2014).

Rivers are often considered to be the dominant source of dissolved Ba in the ocean (Edmond et al., 1978; Wolgemuth & Broecker, 1970). Estimated Ba fluxes from rivers, including desorption from suspended particulate matter, range from 10 to 20 Gmol y^{-1} for the global ocean (Bridgestock et al., 2021; Mayfield et al., 2021; Paytan & Kastner, 1996; Rahaman & Singh, 2023; Rahman et al., 2022). About 20% of the global river discharges enter the Pacific (Meybeck & Ragu, 1997). Scaling that fraction leads to a riverine Ba flux of 2–4 Gmol y^{-1}. Scaling to the area of the Pacific yields a flux estimate of +18 ± 9 μmol m^{-2} y^{-1}. The global flux of Ba from freshwater SGD is estimated between 0.4 Gmol y^{-1} and 3.6 Gmol y^{-1} (Mayfield et al., 2021). Scaling this using the same procedure as the SGD ^{226}Ra source translates to 2.5–22.3 μmol m^{-2} y^{-1} for the Pacific. These estimations do not take into account the circulation of seawater through coastal sediments, which represents an even more important component of SGD and has been shown to provide Ba inputs that exceed riverine Ba inputs in certain regions (Moore, 1997; Moore & Shaw, 2008; Shaw et al., 1998). Rahman et al. (2022) estimated the total SGD (freshwater and saltwater) inputs for Ba to be 17 Gmol y^{-1}, which translates to 47 μmol m^{-2} y^{-1} for the Pacific. The average estimated flux for SGD (fresh and saltwater) is +15 ± 22 μmol m^{-2} y^{-1}.

4.3.3. Hydrothermal

From 5°N to 20°S (stations 27 to 39), higher ^{226}Ra anomalies (2–16 dpm 100 L^{-1}) are observed at ≈2,500 m. Kipp, Sanial, et al. (2018) also observed ^{226}Ra anomalies between 2 and 3 dpm 100 L^{-1} above the TAG hydrothermal vent in the Atlantic Ocean (St. 16 of GA03) and above the East Pacific Rise (St. 18 of GP16). The presence of ^{226}Ra anomalies in our data may be explained by the hydrothermal vent plumes from the East Pacific Rise. Hydrothermal circulating fluids are enriched in radionuclides, such as radium, during the circulation of seawater through the crust via water-rock reactions (Cochran, 1982; Kadko & Moore, 1988). The hydrothermal

Global Biogeochemical Cycles

10.1029/2023GB008005

Table 1
^{226}Ra and Ba Fluxes in the Pacific in dpm m^{-2} y^{-1} and µmol m^{-2} y^{-1}, Respectively

Flux	^{226}Ra (dpm m^{-2} y^{-1})			Ba (µmol m^{-2} y^{-1})			References
Surface							
Rivers	11	±	7	18	±	9	(Bridgestock et al., 2021; Edmond et al., 1978; Mayfield et al., 2021; Rahaman & Singh, 2023; Rahman et al., 2022)
Submarine Groundwater Discharge (fresh and saltwater)	130	±	46	15	±	22	(Mayfield et al., 2021; Rahman et al., 2022)
Export	−358	±	153	−284	±	143	(Moore & Dymond, 1991)
Transport upward	174	±	150	56	±	35	(Talley et al., 2011a)
Transport downard	−66	±	71	−17	±	11	(Talley et al., 2011a)
Radioactive decay	−45			N/A			
Net (Inputs-Losses)	−175 ± 121			−208 ± 73			
Deep							
Export	358	±	153	284	−	143	(Moore & Dymond, 1991)
Transport upward	−174	±	150	−56	±	35	(Talley et al., 2011a)
Transport downard	66	±	71	17	±	11	(Talley et al., 2011a)
Hydrothermal vents	<0.1			<0.1			(Elderfield & Schultz, 1996; Kipp, Sanial, et al., 2018; Nielsen et al., 2006)
Benthic flux (Dissolution and ^{226}Ra from ^{230}Th	1,449	±	502	176	±	243	(Carter et al., 2020; Cochran, 1980; Dehairs et al., 1980; Kemnitz et al., 2023; Steiner et al., 2023)
Burial	−94	±	44	−78	±	82	(Hayes et al., 2021; Moore & Dymond, 1991)
Radioactive decay	−425			N/A			
Net (Inputs-Losses)	916 ± 264			170 ± 106			

activity also introduces significant quantities of ^{3}He-rich into the deep ocean basins, which can be used to trace the hydrothermal buoyant plumes (Jenkins et al., 2018; Lupton, 1998).

Hydrothermal activity in the Pacific generates intense helium plumes distributed by regional circulation between 2,000 m and 3,000 m, extending westward from the East Pacific Rise into the Pacific Basin (Jenkins et al., 2018; Lupton, 1998). Along the GP15 transect, from 20°N to 20°S, excess helium-3 ($^{3}He_{xs}$) concentrations increase (>0.8 fM) between 2,000 m and 3,000 m. High $^{3}He_{xs}$ confirm the presence of neutrally buoyant hydrothermal plumes from the East Pacific Rise (Jenkins & German, 2021a, 2021b). The global water flux of hydrothermal vents is estimated to range between 0.17 and 4.4 10^{10} m^3 y^{-1} (Elderfield & Schultz, 1996; Nielsen et al., 2006). Assuming 46% of these water fluxes enter the Pacific, with ^{226}Ra activities ranging from 220 to 7,300 dpm m^{-3} (Kipp, Sanial, et al., 2018), and dividing by the area of the Pacific yields hydrothermal plume inputs of less than 0.2 dpm m^{-2} y^{-1}, although these inputs may cause local anomalies.

In contrast, Ba seems to be less influenced by hydrothermal inputs, as no higher Ba anomalies are observed at these locations or anywhere along GP15. Furthermore, the ^{226}Ra/Ba ratios at these locations are higher (up to 3.51 dpm μmmol^{-1}) than the average ratio of 2.3 dpm μmmol^{-1}. While hydrothermal fluids carry significant quantities of Ba (von Damn et al., 1985), much of this is thought to precipitate as $BaSO_4$ upon mixing with sulfate-rich seawater, as in cold seeps (Dickens, 2001; Torres et al., 1996). Minerals with elevated Ba concentrations are also likely to sequester some Ra, with potential candidates including barite, calcite, celestite, and brucite (Moore et al., 2021). Recent studies indicate that hydrothermal Ba release contributes, at most, 10% of the total Ba input to the Atlantic (Hsieh et al., 2021), although the impact may be far less (e.g., Bridgestock et al., 2021). Notably, a detailed analysis of Ba budgets by Rahman et al. (2022) revealed no significant influence from hydrothermalism along either GEOTRACES GA03 or GP16. Hence, we believe it is reasonable to assume that the hydrothermal flux of dissolved Ba to the Pacific is negligible.

4.3.4. Sedimentary

Anomalies in ^{226}Ra and Ba concentrations within 2,000 m of the seafloor are likely associated with the dissolution of particles—either occurring in the water column, at the sediment–water interface, or deeper in the sediment pile, with the latter two scenarios manifesting as benthic inputs. A net flux from sediments to the overlaying waters is due to the higher concentrations in pore waters relative to bottom water, leading to a diffusive flux of ^{226}Ra (Cochran, 1980) and Ba (Paytan & Kastner, 1996). ^{226}Ra has an additional source compared to Ba through the decay of sediment-bound ^{230}Th. Once formed, it is released into the overlying waters through diffusion, bioturbation, and sediment resuspension (Cochran & Krishnaswami, 1980; Kemnitz et al., 2023).

Bioturbation of the upper few centimeters of deep-sea sediments produces a mixed zone, with sediment ages estimated to be at least 3,000 years based on ^{14}C dating (DeMaster et al., 1994). Particles within this zone are expected to have a lower ^{226}Ra/Ba ratio compared to settling particles due to almost two half-lives of ^{226}Ra decay. There may also be preferential desorption of Ra compared to Ba (van Beek et al., 2007). Paytan et al. (1996) separated barite from equatorial Pacific sediment cores and measured average ^{226}Ra/Ba ratios of 0.25 ± 0.04 and 0.26 ± 0.04 dpm μmol^{-1} in 4 samples from the upper 3 cm in each core. These ratios are considerably lower than in particles collected in deep sediment traps near the same location of 1.1 to 1.3 dpm μmol^{-1} (Moore & Dymond, 1991), emphasizing the importance of the benthic mixed zone in regulating the ^{226}Ra/Ba ratio released from dissolving barite.

The diffusion of ^{226}Ra from sediment varies depending on sediment composition (Cochran, 1980; Kemnitz et al., 2023). The GP15 section crosses different types of sediments, including red clays as well as radiolarian and calcareous oozes with some siliceous mud (Dutkiewicz et al., 2015). The longer a water mass is in contact with the sediments, the more ^{226}Ra and Ba may accumulate in that water mass. Indeed, the preservation of Ba in the sediment ranges from 30% to 40% of the overlying water column production, so 60% to 70% of the previously calculated rain of water column Ba may redissolve (Paytan & Kastner, 1996; Rahman et al., 2022).

Kemnitz et al. (2023) estimated benthic ^{226}Ra fluxes in the North Pacific along the C-Disk-IV transect of between 720 and 1,690 dpm m^{-2} y^{-1}. The fluxes were calculated by fitting a reaction-transport model for ^{226}Ra based on ^{230}Th concentrations and ^{226}Ra profiles in the upper sediment column. Cochran (1980) estimated a similar ^{226}Ra sediment flux ranging between 22 and 2100 dpm m^{-2} y^{-1} for the North Equatorial Pacific. At most sites, this flux is far larger than expected from the dissolution of barite and must be dominated by ^{226}Ra produced by ^{230}Th

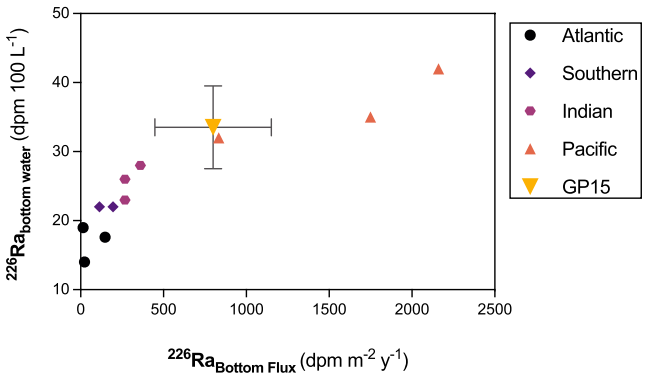

Figure 7. ^{226}Ra bottom fluxes in relationship with the bottom water ^{226}Ra activities determined in different oceanic basins from Cochran (1980) and Kemnitz et al. (2023) data.

decay. Furthermore, Kemnitz et al. (2023) sites had bioturbated layers with mean ages exceeding 10 ky, so barite dissolution there would release negligible ^{226}Ra. While ^{226}Ra benthic flux is mostly derived from ^{230}Th decay, Ba benthic flux is mostly due to barite dissolution. The global Ba dissolution fluxes have been estimated to be +176 ± 243 μmol m^{-2} y^{-1} (Carter et al., 2020; Dehairs et al., 1980; Steiner et al., 2023). The most significant barite dissolution is expected to occur below 4,000 m, as Pacific seawater is saturated for barite above that depth (Mete et al., 2023). Shallower supersaturation may prevent barite from dissolving and releasing Ba and ^{226}Ra into intermediate waters.

4.4. Synthesis

We employed data from this study and previous process studies to construct a comprehensive ^{226}Ra and Ba budget for the Pacific Ocean. Our aim was to assess the relative significance of various sources and sinks in shaping the oceanic distributions of ^{226}Ra and Ba. The budget accounts for terrestrial sources such as rivers and submarine groundwater discharge, inputs from hydrothermal vents and sediment fluxes, vertical mixing, losses from radioactive decay, and removal through the particulate flux, including redissolution in deep water (Figure 7). To simplify the budget calculation, we considered the Pacific Ocean in terms of two boxes—a surface box extending from the surface to 1,000 m, and a deep box from 1,000 m to the seafloor. We used an average depth of 4,280 m and an area of 1.62×10^{14} m^2 for the Pacific (Costello et al., 2015). This division helps simplify the calculation of ^{226}Ra and Ba sinks and sources, which sometimes operate in only a single box.

4.4.1. Intra-Pacific Fluxes

In constructing our mass balance, we must also account for fluxes of ^{226}Ra and Ba between the shallow and deep boxes. For example, particulate formation plays a crucial role in maintaining low ^{226}Ra activities and Ba concentrations near the surface, which moves these two elements into the deep box. However, particle removal is counteracted by upward mixing, though in the Pacific this term is minor. The average export flux of ^{226}Ra and Ba estimated by Moore and Dymond (1991) from sediment traps (between 500 and 1,500 m deep) in the equatorial Pacific ranged from 216 to 668 dpm m^{-2} y^{-1} and from 146.0 to 418.0 μmol m^{-2} y^{-1} respectively (Figure 7).

A weak overturning cell is found in the North Pacific, forming a small amount (1.5 Sv (10^6 m^3 s^{-1}) to 3.9 Sv) of the NPIW (Talley, 2013). This cell provides the surface with relatively rich ^{226}Ra and Ba water and deep waters with low ^{226}Ra and Ba waters. Along the GP15 transect, the average deep ^{226}Ra activities and Ba concentrations are 30.3 ± 6.8 and 124.9 ± 18.9 nmol L^{-1}, respectively. Along GP15, the average surface ^{226}Ra activities and Ba concentrations are 10.3 ± 5.0 and 50.4 ± 17.9 nmol L^{-1}, respectively. An area of 1.62×10^{14} m^2 was used to estimate the transport from the deep compartment to the surface. Thus, the upward flux in the NPIW cell system ranges from 68 to 280 dpm m^{-2} y^{-1} for ^{226}Ra and from 31 to 81 μmol m^{-2} y^{-1} for Ba. The downward flux downward in the system ranges from 16 to 116 dpm m^{-2} y^{-1} for ^{226}Ra and from 10 to 25 μmol m^{-2} y^{-1} for Ba.

4.4.2. Net Benthic Fluxes

Assuming that the accumulation of ^{226}Ra and Ba in deep-water masses is entirely due to bottom sources such as sediment diffusion or dissolution of particles, the excess ^{226}Ra and Ba anomalies can be converted into bottom fluxes (F_{bottom}) using Equation 4 for Ba and Equation 5 for ^{226}Ra.

$$F_{\mathrm{Ba-bottom}} = \frac{Xi \times h}{t} \quad (4)$$

$$F_{\mathrm{Ra-bottom}} = \frac{X_i \times h}{\tau} + \lambda \times [\mathrm{Ra}] \times h \quad (5)$$

where X_i is the average anomaly of ^{226}Ra or Ba (in dpm m^{-3} or nmol m^{-3}) in the lower 2,000 m of the water column along GP15, h is the water column thickness (2,000 m), τ. the water residence time in the deep North

Pacific (596 years from Matsumoto, 2007), and λ is the decay constant for ^{226}Ra. ^{226}Ra bottom fluxes required to explain the ^{226}Ra anomalies observed along the GP15 is +799 ± 351 dpm m^{-2} y^{-1} (Figure 7). These fluxes are within the range of fluxes reported in the literature (Figure 7a). Sedimentary fluxes in the range of 15 dpm m^{-2} to 2160 dpm m^{-2} y^{-1} (Figure 7; Cochran, 1980; Kemnitz et al., 2023; Le Roy et al., 2018; Li et al., 1973; Rutgers van der Loeff et al., 2018). Li et al. (1973) estimated ^{226}Ra fluxes diffusing out of the sediment in the Southern Ocean and on the Antarctic shelf of +6.2 and +16 dpm m^{-2} y^{-1}, respectively.

Bottom fluxes for Ba of +95 ± 61 μmol m^{-2} y^{-1} would be required to explain the Ba anomalies observed along GP15 (Figure 7). These fluxes are on the high end of Ba sedimentary fluxes reported in different ocean basins, which range from 0.21 to 400 μmol m^{-2} y^{-1} (Chan et al., 1976, 1977; Falkner et al., 1993; McManus et al., 1999; Paytan & Kastner, 1996; Steiner et al., 2023). While our estimated benthic fluxes are toward the higher end of published values, it is important to keep in mind that our flux calculation considers water column *and* sedimentary $BaSO_4$ dissolution as a single benthic flux. In contrast, previous studies considered these terms separately, resulting in generally lower benthic fluxes. Given the results of Steiner et al. (2023), who observed benthic Ba fluxes of up to 95 μmol m^{-2} y^{-1} in the North Pacific, our data indicate that between 25% and 100% of the observed Ba flux originates from sediments with the balance from the water column dissolution. Variations in ^{226}Ra and Ba fluxes released from the bottom may be due to differences in sedimentary ^{230}Th activity, bioturbation rates, sediment type and composition, and may also vary as a function of surface productivity, particle export and burial.

Cochran (1980) showed an inverse relation between flux and sedimentation rate, with rapidly accumulating sediments having the lowest ^{226}Ra fluxes. The main explanation is that particles arriving at the seafloor in high-productivity areas have accumulated lower concentrations of excess ^{230}Th while sinking through the water column and therefore have lower production rates of ^{226}Ra near the sediment-water interface. In the Pacific, the sedimentation rates are higher near the margin (up to ∼8 g cm^{-2} ky^{-1}; Costa et al., 2020), which corresponds with the lowest bottom fluxes observed near the Alaskan margin for ^{226}Ra.

Benthic Ba fluxes also exhibit systematic spatial variations. For example, benthic Ba fluxes are typically high along the continental margin, where Ba is rapidly remobilized during suboxic sedimentary diagenesis (e.g., McManus et al. (1999)). Barium remobilization also occurs in the deep ocean albeit at slower rates. Despite the slower rates, there are still clear meridional trends in Ba benthic fluxes. Paytan and Kastner (1996) observed the highest fluxes centered on the Equator, where it is thought that the higher productivity in the divergence zone leads to a larger flux of particulate Ba toward the sediment, leading to higher Ba accumulation. Sediments beneath regions of high primary productivity often exhibit enrichment in Ba-bearing solid phases (e.g., Brumsack, 1989; Goldberg & Arrhenius, 1958; Nürnberg et al., 1997; Paytan & Kastner, 1996), though few flux measurements exist.

Similar to ^{226}Ra diffusion from sediments, Ba regeneration appears sensitive to sediment accumulation rate: rapid burial will shorten the period during which the Ba-rich sediment is exposed to bottom waters, thereby increasing the preservation of barite (Dymond et al., 1992). However, the anomalies in our dataset, with negative in the top 2,000 m and positive below, indicate significant Ba inputs from $BaSO_4$ dissolution in the deep Pacific Basin. This is somewhat surprising given that the majority of the Pacific Ocean below 1,000 m is at—or even exceeds—saturation equilibrium with respect to $BaSO_4$ (Figure 5; Mete et al., 2023). We propose three possible explanations for this behavior. First, $BaSO_4$ solubility increases with increasing pressure (Monnin et al., 1999). Thus, a significant fraction of the Pacific seafloor is undersaturated with respect to $BaSO_4$ and dissolution is thermodynamically favored. Second, it is possible that pelagic $BaSO_4$ dissolution does occur in the water column despite ambient supersaturation. One putative mechanism could be the development of $BaSO_4$-undersaturated microenvironments within the $BaSO_4$-supersaturated water column. Such microenvironments would be analogous to those hypothesized to contribute to $BaSO_4$ precipitation in the $BaSO_4$-understated shallow ocean, and an equivalent mechanism was recently proposed by Subhas et al. (2023) to explain shallow $CaCO_3$ dissolution in the Pacific Ocean. Third, it is possible that pelagic $BaSO_4$ solubility differs from thermodynamic predictions based on experiments with well-crystalized barite. Possible reasons for such differences could include $BaSO_4$ morphology (Light, Martínez-Ruiz et al., 2023), the presence of organic matter (Light, Garcia, et al., 2023), or uncertainties in the underlying thermodynamic model (see Mete et al., 2023, for a discussion). Though we are not able to identify the primary driver of $BaSO_4$ dissolution in this region, our results are consistent with prior research evidencing considerable benthic $BaSO_4$ fluxes within the Pacific Basin.

4.4.3. Net ^{226}Ra and Ba Fluxes in the Pacific Basin

The characterization and estimation of ^{226}Ra and Ba input and removal fluxes allow us to better understand the ^{226}Ra and Ba relationships in the Pacific Ocean. Each term has been independently estimated, and no attempt is made to balance the fluxes. Net fluxes and their associated uncertainties were estimated using a Monte Carlo simulation. Following a normal distribution, one hundred million possible values were generated within each flux range of estimations. The only parameters considered unique are the ^{226}Ra decay fluxes.

Considering all fluxes, the sum of all inputs and losses in the surface box yields a net flux of -175 ± 121 dpm m^{-2} y^{-1} for ^{226}Ra and -208 ± 73 μmol m^{-2} y^{-1} for Ba. Similarly, for the deep Pacific Ocean, there is a net accumulation of $+916 \pm 264$ dpm m^{-2} y^{-1} for ^{226}Ra and $+170 \pm 106$ μmol m^{-2} y^{-1} for Ba. These balances suggest that Ra and Ba sources may be underestimated in the surface and overestimated in the deep.

The main contributor of Ba to the surface ocean in the Pacific is the upward transport of deeper waters. Rivers and SGD inputs, on average, represent 21% and 17% of the total surface Ba input fluxes, respectively. Despite this, the global significance of saline SGD and its role in contributing Ba to the ocean remains poorly constrained, and may be underestimated (Rahaman & Singh, 2023; Rahman et al., 2022). Export is larger than all incoming Ba sources in the North Pacific, leading to a net deficit in the surface, consistent with large negative Ba anomalies in the top 2,000 m along GP15. For ^{226}Ra, SGD is the main source to the surface, accounting for 65% of the inputs. The surface ^{226}Ra budget is close to balanced and consistent with the anomalies observed in the surface along the section.

In deep-water budgets, the hydrothermal fluxes are low, representing less than 0.1% of the total inputs for ^{226}Ra and Ba, respectively. The dissolution of $BaSO_4$ is the main Ba source in the deep-water mass balance. Given the nature of our approach, we cannot ascribe a specific depth for this source. However, we note that the Pacific water column between 1,000 m and 4,000 m generally seems to exceed saturation with respect to $BaSO_4$ (Mete et al., 2023), whereas deeper waters are slightly undersaturated. If thermodynamics is the dominant process governing $BaSO_4$ dissolution, most $BaSO_4$ dissolution must occur close to, or below, the seafloor. Alternatively, $BaSO_4$ dissolution might occur throughout the water column, including in $BaSO_4$ supersaturated waters. Regardless, $BaSO_4$ dissolution effectively balances the removal terms and is consistent with the positive Ba anomalies observed along the section.

In the deep Pacific, the excess of ^{226}Ra is primarily driven by the low rates of burial and decay relative to particle dissolution and production in the sediment. This aligns with the deep positive anomalies and the estimated bottom flux; however, the calculated excess of ^{226}Ra could potentially lead to ^{226}Ra activities in the global ocean that surpass current estimates. Even if the North Equatorial Pacific is known to be a net source of ^{226}Ra to the world's oceans (Cochran, 1980), the fluxes reported here may not be representative of the whole Pacific. Alternatively, removal of excess Pacific ^{226}Ra may occur during return flow through the Southern Ocean hub associated with the biological pump. The Southern Ocean is a major sink for biogenic silica (DeMaster et al., 1992; Tréguer, 2014) and the depletion of ^{226}Ra in the surface of the Southern Ocean has been attributed to siliceous tests acting as carriers for radium (Edmond, 1970; Ku et al., 1970). If correct, the Southern Ocean may play a crucial role in regulating ^{226}Ra activities in the global ocean, potentially impacting its overall budget and distribution.

5. Conclusion

We explore the distribution and influencing factors affecting ^{226}Ra and Ba along the GEOTRACES GP15 section in the Pacific Ocean. We apportion the relative importance of conservative and non-conservative processes using a water mass analysis. We find that physical circulation—conservative processes—explains around half of the ^{226}Ra distribution and two thirds of the Ba distribution. The balance derives from non-conservative processes, which are identified based on the direction and magnitude of deviations between their expected and observed distributions. In the top 2,000 m, large deficits of ^{226}Ra and Ba are observed, likely resulting from the transfer of ^{226}Ra and Ba from the dissolved phase to particles, such as barite. These deficits extend below the mesopelagic region, implying either considerable barite formation occurred in these waters between their surface source region and the GP15 section, or that there is extensive deep barite precipitation in the North Pacific. Below 2,000 m, both ^{226}Ra and Ba show extensive positive anomalies, which must be sustained by a combination of surface-derived particle dissolution and benthic inputs. Disparities between ^{226}Ra and Ba can be attributed to the spatial differences of their sources and the slow mixing in some parts of the deep Pacific. We use a mass balance to estimate

net ^{226}Ra and Ba fluxes, which reveals that the most important source of ^{226}Ra to the deep Pacific is the release of ^{226}Ra from sediments, which likely explains the elevated ^{226}Ra/Ba in the deepest waters. These calculations also reveal a net deficit in Ba sources, with the caveat that there is considerable uncertainty concerning the flux of Ba from submarine groundwater discharge into surface waters. A key goal of future studies will be to understand the mechanisms and quantify the rates of particle dissolution in barite-supersaturated environments, to discern the fate of the excess ^{226}Ra exported from the Pacific Ocean, and to constrain Ba fluxes to the surface Pacific Ocean.

Data Availability Statement

All the datasets measured are available on the BCO-DMO website (Charette & Moore, 2023a, 2023b; Shiller, 2021a, 2021b).

Acknowledgments
The authors thank the GEOTRACES GP15 cruise leaders as well as the captain and crew of the R/V *Roger Revelle* for their many efforts that made obtaining this dataset possible. Sample collection was aided by members of the pumping group: Phoebe Lam, Steve Pike, Yang Xiang, Vinicius Amaral, and Jennifer Kenyon. This study was funded by the National Science Foundation through Grants to W. S.M. (OCE-1736321), M.A.C., (OCE-1736277), A.M.S. (OCE-1737024), and T. J.H. (OCE-1736949 and OCE-2048604). E.L.R. was supported by a postdoctoral scholarship from the Center for Marine and Environmental Radioactivity.

References

Arzel, O., & Verdière, A. C. D. (2016). Can we infer diapycnal mixing rates from the world ocean temperature–salinity distribution? *Journal of Physical Oceanography*, *46*(12), 3751–3775. https://doi.org/10.1175/JPO-D-16-0152.1

Beaulieu, S. E., & Szafranski, K. (2020). InterRidge global database of active submarine hydrothermal vent fields. Retrieved from http://vents-data.interridge.org

Bernstein, R. E., Betzer, P. R., Feely, R. A., Byrne, R. H., Lamb, M. F., & Michaels, A. F. (1987). Acantharian fluxes and strontium to chlorinity ratios in the North Pacific Ocean. *Science*, *237*(4821), 1490–1494. https://doi.org/10.1126/science.237.4821.1490

Bernstein, R. E., & Byrne, R. H. (2004). Acantharians and marine barite. *Marine Chemistry*, *86*(1–2), 45–50. https://doi.org/10.1016/j.marchem.2003.12.003

Bernstein, R. E., Byrne, R. H., Betzer, P. R., & Greco, A. M. (1992). Morphologies and transformations of celestite in seawater: The role of acantharians in strontium and barium geochemistry. *Geochimica et Cosmochimica Acta*, *56*(8), 3273–3279. https://doi.org/10.1016/0016-7037(92)90304-2

Bertram, M. A., & Cowen, J. P. (1997). Morphological and compositional evidence for biotic precipitation of marine barite. *Journal of Marine Research*, *55*(3), 577–593. https://doi.org/10.1357/0022240973224292

Bian, X., Yang, S.-C., & John, S. G. (2022a). Dissolved concentrations of nickel and copper from bottle samples collected on Leg 1 (Seattle, WA to Hilo, HI) of the US GEOTRACES Pacific Meridional Transect (PMT) cruise (GP15, RR1814) on R/V Roger Revelle from September to October 2018 (Version 1) [Dataset]. *Biological and Chemical Oceanography Data Management Office (BCO-DMO)*. https://doi.org/10.26008/1912/BCO-DMO.885319.1

Bian, X., Yang, S.-C., & John, S. G. (2022b). Dissolved concentrations of nickel and copper from bottle samples collected on Leg 2 (Hilo, HI to Papeete, French Polynesia) of the US GEOTRACES Pacific Meridional Transect (PMT) cruise (GP15, RR1815) on R/V Roger Revelle from October to November 2018 (Version 1) [Dataset]. *Biological and Chemical Oceanography Data Management Office (BCO-DMO)*. https://doi.org/10.26008/1912/BCO-DMO.885335.1

Bishop, J. K. B. (1988). The barite-opal-organic carbon association in oceanic particulate matter. *Nature*, *332*(6162), 341–343. https://doi.org/10.1038/332341a0

Bograd, S. J., Schroeder, I. D., & Jacox, M. G. (2019). A water mass history of the Southern California current system. *Geophysical Research Letters*, *46*(12), 6690–6698. https://doi.org/10.1029/2019GL082685

Bridgestock, L., Nathan, J., Paver, R., Hsieh, Y.-T., Porcelli, D., Tanzil, J., et al. (2021). Estuarine processes modify the isotope composition of dissolved riverine barium fluxes to the ocean. *Chemical Geology*, *579*, 120340. https://doi.org/10.1016/j.chemgeo.2021.120340

Broecker, W., Kaufman, A., Ku, T.-L., Chung, Y.-C., & Craig, H. (1970). Radium 226 measurements from the 1969 North Pacific Geosecs Station. *Journal of Geophysical Research*, *75*(36), 7682–7685. https://doi.org/10.1029/JC075i036p07682

Broecker, W. S., Li, Y.-H., & Cromwell, J. (1967). Radium-226 and Radon-222: Concentration in Atlantic and Pacific Oceans. *Science*, *158*(3806), 1307–1310. https://doi.org/10.1126/science.158.3806.1307

Brumsack, H.-J. (1989). Geochemistry of recent TOC-rich sediments from the Gulf of California and the Black Sea. *Geologische Rundschau*, *78*(3), 851–882. https://doi.org/10.1007/BF01829327

Bullock, E. J., Kipp, L., Moore, W., Brown, K., Mann, P. J., Vonk, J. E., et al. (2022). Radium inputs into the Arctic Ocean from rivers: A basin-wide estimate. *Journal of Geophysical Research: Oceans*, *127*(9), e2022JC018964. https://doi.org/10.1029/2022JC018964

Carter, S. C., Paytan, A., & Griffith, E. M. (2020). Toward an improved understanding of the marine barium cycle and the application of marine barite as a paleoproductivity proxy. *Minerals*, *10*(5), 421. https://doi.org/10.3390/min10050421

Chan, L. H., Drummond, D., Edmond, J. M., & Grant, B. (1977). On the barium data from the Atlantic GEOSECS expedition. *Deep-Sea Research*, *24*(7), 613–649. https://doi.org/10.1016/0146-6291(77)90505-7

Chan, L. H., Edmond, J. M., Stallard, R. F., Broecker, W. S., Chung, Y. C., Weiss, R. F., & Ku, T. L. (1976). Radium and barium at GEOSECS stations in the Atlantic and Pacific. *Earth and Planetary Science Letters*, *32*(2), 258–267. https://doi.org/10.1016/0012-821x(76)90066-2

Charette, M. A., Buesseler, K. O., & Andrews, J. E. (2001). Utility of radium isotopes for evaluating the input and transport of groundwater-derived nitrogen to a Cape Cod estuary. *Limnology & Oceanography*, *46*(part 2), 465–470. https://doi.org/10.4319/lo.2001.46.2.0465

Charette, M. A., & Moore, W. S. (2023a). Water column dissolved radium-226 and radium-228 from Leg 1 (Seattle, WA to Hilo, HI) of the US GEOTRACES Pacific Meridional Transect (PMT) cruise (GP15, RR1814) on R/V Roger Revelle from September to October 2018. (Version 3) Version Date 2023-10-02. *Biological and Chemical Oceanography Data Management Office (BCO-DMO)*. https://doi.org/10.26008/1912/bco-dmo.825891.3

Charette, M. A., & Moore, W. S. (2023b). Water column dissolved radium-226 and radium-228 from Leg 2 (Hilo, HI to Papeete, French Polynesia) of the US GEOTRACES Pacific Meridional Transect (PMT) cruise (GP15, RR1815) on R/V Roger Revelle from October to November 2018. (Version 3) Version Date 2023-10-02. *Biological and Chemical Oceanography Data Management Office (BCO-DMO)*. https://doi.org/10.26008/1912/bco-dmo.825947.3

Charette, M. A., Morris, P. J., Henderson, P. B., & Moore, W. S. (2015). Radium isotope distributions during the US GEOTRACES North Atlantic cruises. *Marine Chemistry*, *177*(Part 1), 184–195. https://doi.org/10.1016/j.marchem.2015.01.001

Cherry, R. D. (1964). Alpha-radioactivity of plankton. *Nature*, *203*(4941), 139–143. https://doi.org/10.1038/203139a0

Chow, T. J., & Goldberg, E. D. (1960). On the marine geochemistry of barium. *Geochimica et Cosmochimica Acta*, *20*(3–4), 192–198. https://doi.org/10.1016/0016-7037(60)90073-9

Chung, Y. (1980). Radium-barium-silica correlations and a two-dimensional radium model for the world ocean. *Earth and Planetary Science Letters*, *49*(2), 309–318. https://doi.org/10.1016/0012-821X(80)90074-6

Chung, Y., Craig, H., Ku, T. L., Goddard, J., & Broecker, W. S. (1974). Radium-226 measurements from three Geosecs intercalibration stations. *Earth and Planetary Science Letters*, *23*(1), 116–124. https://doi.org/10.1016/0012-821X(74)90038-7

Chung, Y.-C., & Craig, H. (1980). ^{226}Ra in the Pacifique Ocean. *Earth and Planetary Science Letters*, *49*(2), 267–292. https://doi.org/10.1016/0012-821x(80)90072-2

Cochran, J. K. (1980). The flux of ^{226}Ra from deep-sea sediments. *Earth and Planetary Science Letters*, *49*(2), 381–392. https://doi.org/10.1016/0012-821X(80)90080-1

Cochran, J. K. (1982). *The oceanic chemistry of the U- and Th-series nuclides*. Oxford University Press.

Cochran, J. K., & Krishnaswami, S. (1980). Radium, thorium, uranium, and ^{210}Pb in deep-sea sediments and sediment pore waters from the North Equatorial Pacific. *American Journal of Science*, *280*(9), 849–889. https://doi.org/10.2475/ajs.280.9.849

Costa, K. M., Hayes, C. T., Anderson, R. F., Pavia, F. J., Bausch, A., Deng, F., et al. (2020). ^{230}Th normalization: New insights on an essential tool for quantifying sedimentary fluxes in the modern and quaternary ocean. *Paleoceanography and Paleoclimatology*, *35*(2), e2019PA003820. https://doi.org/10.1029/2019PA003820

Costello, M. J., Cheung, A., & De Hauwere, N. (2015). Topographic statistics for the surface and seabed area, volume, depths, and slopes for the world's seas, oceans and countries (other). https://doi.org/10.14293/P2199-8442.1.SOP-LIFE.PZDAWX.v1

Dehairs, F., Baeyens, W., & Goeyens, L. (1992). Accumulation of suspended barite at mesopelagic depths and export production in the Southern Ocean. *Science*, *258*(5086), 1332–1336. https://doi.org/10.1126/science.258.5086.1332

Dehairs, F., Chesselet, R., & Jedwab, J. (1980). Discrete suspended particles of barite and the barium cycle in the open ocean. *Earth and Planetary Science Letters*, *49*(2), 528–550. https://doi.org/10.1016/0012-821X(80)90094-1

Dehairs, F., Goeyens, L., Stroobants, N., Bernard, P., Goyet, C., Poisson, A., & Chesselet, R. (1990). On suspended barite and the oxygen minimum in the Southern Ocean. *Global Biogeochemical Cycles*, *4*(1), 85–102. https://doi.org/10.1029/GB004i001p00085

Dehairs, F., Shopova, D., Ober, S., Veth, C., & Goeyens, L. (1997). Particulate barium stocks and oxygen consumption in the Southern Ocean mesopelagic water column during spring and early summer: Relationship with export production. *Deep Sea Research Part II: Topical Studies in Oceanography*, *44*(1), 497–516. https://doi.org/10.1016/S0967-0645(96)00072-0

DeMaster, D., Dunbar, R., Gordon, L., Leventer, A., Morrison, J., Nelson, D., et al. (1992). Cycling and accumulation of biogenic silica and organic matter in high-latitude environments: The Ross Sea. *Oceanography*, *5*(3), 146–153. https://doi.org/10.5670/oceanog.1992.03

DeMaster, D. J., Pope, R. H., Levin, L. A., & Blair, N. E. (1994). Biological mixing intensity and rates of organic carbon accumulation in North Carolina slope sediments. *Deep Sea Research Part II: Topical Studies in Oceanography*, *41*(4), 735–753. https://doi.org/10.1016/0967-0645(94)90045-0

Dickens, G. R. (2001). Sulfate profiles and barium fronts in sediment on the Blake Ridge: Present and past methane fluxes through a large gas hydrate reservoir. *Geochimica et Cosmochimica Acta*, *65*(4), 529–543. https://doi.org/10.1016/S0016-7037(00)00556-1

Dickens, G. R., Fewless, T., Thomas, E., & Bralower, T. J. (2003). Excess barite accumulation during the Paleocene-Eocene thermal Maximum: Massive input of dissolved barium from seafloor gas hydrate reservoirs. In S. L. Wing, P. D. Gingerich, B. Schmitz, & E. Thomas (Eds.), *Causes and consequences of globally warm climates in the early Paleogene* (Vol. 369, p. 0). Geological Society of America. https://doi.org/10.1130/0-8137-2369-8.11

Dutkiewicz, A., Müller, R. D., O'Callaghan, S., & Jónasson, H. (2015). Census of seafloor sediments in the world's ocean. *Geology*, *43*(9), 795–798. https://doi.org/10.1130/G36883.1

Dymond, J., Suess, E., & Lyle, M. (1992). Barium in deep-sea sediment: A geochemical proxy for paleoproductivity. *Paleoceanography*, *7*(2), 163–181. https://doi.org/10.1029/92PA00181

Edmond, J. M. (1970). Comments on the paper by T. L. Ku, Y. H. Li, G. G. Mathieu, and H. K. Wong, radium in the Indian–Antarctic Ocean south of Australia. *Journal of Geophysical Research*, *75*(33), 6878–6883. https://doi.org/10.1029/JC075i033p06878

Edmond, J. M., Boyle, E. D., Drummond, D., Grant, B., & Mislick, T. (1978). Desorption of barium in the plume of the Zaire (Congo) river. *Netherlands Journal of Sea Research*, *12*(3), 324–328. https://doi.org/10.1016/0077-7579(78)90034-0

Elderfield, H., & Schultz, A. (1996). Mid-ocean ridge hydrothermal fluxes and the chemical composition of the ocean. *Annual Review of Earth and Planetary Sciences*, *24*(1), 191–224. https://doi.org/10.1146/annurev.earth.24.1.191

Falkner, K. K., klinkhammer, G. P., Bowers, T. S., Todd, J. F., Lewis, B. L., Landing, W. M., & Edmond, J. M. (1993). The behavior of barium in anoxic marine waters. *Geochimica et Cosmochimica Acta*, *57*(3), 537–554. https://doi.org/10.1016/0016-7037(93)90366-5

Fanning, K. A., Vargo, G. A., Bell-Torres, L., & Young, R. W. (1988). Covariation of reactive solutes in the sea. *Marine Chemistry*, *24*(3–4), 215–238. https://doi.org/10.1016/0304-4203(88)90033-3

Faure, V., & Speer, K. (2012). Deep circulation in the eastern South Pacific Ocean. *Journal of Marine Research*, *70*(5), 748–778. https://doi.org/10.1357/002224012806290714

Foster, D. A., Staubwasser, M., & Henderson, G. M. (2004). ^{226}Ra and Ba concentrations in the Ross Sea measured with multicollector ICP mass spectrometry. *Marine Chemistry*, *87*(1–2), 59–71. https://doi.org/10.1016/j.marchem.2004.02.003

Ganeshram, R. S., & Francois, R. (2003). New insights into the mechanism of barite formation in seawater and implications for barium-based paleoproductivity reconstruction, 7443. In *Presented at the EGS - AGU - EUG joint assembly*.

Ganeshram, R. S., François, R., Commeau, J., & Brown-Leger, S. L. (2003). An experimental investigation of barite formation in seawater. *Geochimica et Cosmochimica Acta*, *67*(14), 2599–2605. https://doi.org/10.1016/S0016-7037(03)00164-9

GEOTRACES Standards and Intercalibration Committee. (2017). Sampling and sample-handling protocols for GEOTRACES cruises. Retrieved from http://www.geotraces.org/images/stories/documents/intercalibration/Cookbook.pdf

Goldberg, E. D., & Gos, A. (1958). Chemistry of Pacific pelagic sediments. *Geochimica et Cosmochimica Acta*, *13*(2), 153–212. https://doi.org/10.1016/0016-7037(58)90046-2

González-Muñoz, M. T., Fernández-Luque, B., Martínez-Ruiz, F., Chekroun, K. B., Arias, J. M., Rodríguez-Gallego, M., et al. (2003). Precipitation of barite by Myxococcus Xanthus: Possible implications for the biogeochemical cycle of barium. *Applied and Environmental Microbiology*, *69*(9), 5722–5725. https://doi.org/10.1128/AEM.69.9.5722-5725.2003

Gonzalez-Muñoz, M. T., Martinez-Ruiz, F., Morcillo, F., Martin-Ramos, J. D., & Paytan, A. (2012). Precipitation of barite by marine bacteria: A possible mechanism for marine barite formation. *Geology*, *40*(8), 675–678. https://doi.org/10.1130/G33006.1

Griffith, E. M., & Paytan, A. (2012). Barite in the ocean – Occurrence, geochemistry and palaeoceanographic applications. *Sedimentology*, *59*(6), 1817–1835. https://doi.org/10.1111/j.1365-3091.2012.01327.x

Hartin, C. A., Fine, R. A., Sloyan, B. M., Talley, L. D., Chereskin, T. K., & Happell, J. (2011). Formation rates of Subantarctic mode water and Antarctic intermediate water within the South Pacific. *Deep Sea Research Part I: Oceanographic Research Papers*, *58*(5), 524–534. https://doi.org/10.1016/j.dsr.2011.02.010

Hatta, M., Measures, C. I., Wu, J., Roshan, S., Fitzsimmons, J. N., Sedwick, P., & Morton, P. (2014). An overview of dissolved Fe and Mn distributions during the 2010–2011 U.S. GEOTRACES North Atlantic cruises: GEOTRACES GA03. *Deep Sea Research Part II: Topical Studies in Oceanography*, *116*, 117–129. https://doi.org/10.1016/j.dsr2.2014.07.005

Hautala, S. L. (2018). The abyssal and deep circulation of the Northeast Pacific Basin. *Progress in Oceanography*, *160*, 68–82. https://doi.org/10.1016/j.pocean.2017.11.011

Hautala, S. L., & Hammond, D. E. (2020). Abyssal pathways and the double silica maximum in the northeast Pacific Basin. *Geophysical Research Letters*, *47*(19), e2020GL089010. https://doi.org/10.1029/2020GL089010

Hayes, C. T., Costa, K. M., Anderson, R. F., Calvo, E., Chase, Z., Demina, L. L., et al. (2021). Global ocean sediment composition and burial flux in the deep sea. *Global Biogeochemical Cycles*, *35*(4), e2020GB006769. https://doi.org/10.1029/2020GB006769

Henderson, P., Morris, P., Moore, W., & Charette, M. (2013). Methodological advances for measuring low-level radium isotopes in seawater. *Journal of Radioanalytical & Nuclear Chemistry*, *296*(1), 357–362. https://doi.org/10.1007/s10967-012-2047-9

Hoppema, M., Dehairs, F., Navez, J., Monnin, C., Jeandel, C., Fahrbach, E., & de Baar, H. J. W. (2010). Distribution of barium in the Weddell Gyre: Impact of circulation and biogeochemical processes. *Marine Chemistry*, *122*(1–4), 118–129. https://doi.org/10.1016/j.marchem.2010.07.005

Horner, T. J., & Crockford, P. W. (2021). *Barium isotopes: Drivers, dependencies, and distributions through space and time* (1st ed.). Cambridge University Press. https://doi.org/10.1017/9781108865845

Horner, T. J., Kinsley, C. W., & Nielsen, S. G. (2015). Barium-isotopic fractionation in seawater mediated by barite cycling and oceanic circulation. *Earth and Planetary Science Letters*, *430*, 511–522. https://doi.org/10.1016/j.epsl.2015.07.027

Horner, T. J., Pryer, H. V., Nielsen, S. G., Crockford, P. W., Gauglitz, J. M., Wing, B. A., & Ricketts, R. D. (2017). Pelagic barite precipitation at micromolar ambient sulfate. *Nature Communications*, *8*(1), 1342. https://doi.org/10.1038/s41467-017-01229-5

Hsieh, Y.-T., Bridgestock, L., Scheuermann, P. P., Seyfried, W. E., & Henderson, G. M. (2021). Barium isotopes in mid-ocean ridge hydrothermal vent fluids: A source of isotopically heavy Ba to the ocean. *Geochimica et Cosmochimica Acta*, *292*, 348–363. https://doi.org/10.1016/j.gca.2020.09.037

Iudicone, D., Rodgers, K. B., Schopp, R., & Madec, G. (2007). An exchange window for the injection of Antarctic intermediate water into the South Pacific. *Journal of Physical Oceanography*, *37*(1), 31–49. https://doi.org/10.1175/JPO2985.1

Jacquet, S. H. M., Dehairs, F., Cardinal, D., Navez, J., & Delille, B. (2005). Barium distribution across the Southern Ocean frontal system in the Crozet-Kerguelen Basin. *Marine Chemistry*, *95*(3–4), 149–162. https://doi.org/10.1016/j.marchem.2004.09.002

Jacquet, S. H. M., Dehairs, F., Elskens, M., Savoye, N., & Cardinal, D. (2007). Barium cycling along WOCE SR3 line in the Southern Ocean. *Marine Chemistry*, *106*(1–2), 33–45. https://doi.org/10.1016/j.marchem.2006.06.007

Jacquet, S. H. M., Lefèvre, D., Tamburini, C., Garel, M., Le Moigne, F. A. C., Bhairy, N., & Guasco, S. (2021). On the barium–oxygen consumption relationship in the Mediterranean Sea: Implications for mesopelagic marine snow remineralization. *Biogeosciences*, *18*(6), 2205–2212. https://doi.org/10.5194/bg-18-2205-2021

Jenkins, W. J., & German, C. R. (2021a). Helium isotope with helium and neon concentration data from Leg 1 (Seattle, WA to Hilo, HI) of the US GEOTRACES Pacific Meridional Transect (PMT) cruise (GP15, RR1814) on R/V Roger Revelle from September to October 2018 (Version 1) [Dataset]. *Biological and Chemical Oceanography Data Management Office (BCO-DMO)*. https://doi.org/10.26008/1912/BCO-DMO.862182.1

Jenkins, W. J., & German, C. R. (2021b). Helium isotope with helium and neon concentration data from Leg 2 (Hilo, HI to Papeete, French Polynesia) of the US GEOTRACES Pacific Meridional Transect (PMT) cruise (GP15, RR1815) on R/V Roger Revelle from Oct-Nov 2018 (Version 1) [Dataset]. *Biological and Chemical Oceanography Data Management Office (BCO-DMO)*. https://doi.org/10.26008/1912/BCO-DMO.862220.1

Jenkins, W. J., Lott, D. E., German, C. R., Cahill, K. L., Goudreau, J., & Longworth, B. (2018). The deep distributions of helium isotopes, radiocarbon, and noble gases along the U.S. GEOTRACES East Pacific Zonal Transect (GP16). *Marine Chemistry*, *201*, 167–182. https://doi.org/10.1016/j.marchem.2017.03.009

Jochem, F. J., Mathot, S., & Quéguiner, B. (1995). Size-fractionated primary production in the open Southern Ocean in austral spring. *Polar Biology*, *15*(6), 381–392. https://doi.org/10.1007/BF00239714

Johnson, G. C., & Toole, J. M. (1993). Flow of deep and bottom waters in the Pacific at 10°N. *Deep Sea Research Part I: Oceanographic Research Papers*, *40*(2), 371–394. https://doi.org/10.1016/0967-0637(93)90009-R

Kadko, D., & Moore, W. (1988). Radiochemical constraints on the crustal residence time of submarine hydrothermal fluids: Endeavour Ridge. *Geochimica et Cosmochimica Acta*, *52*(3), 659–668. https://doi.org/10.1016/0016-7037(88)90328-6

Kemnitz, N., Hammond, D. E., Henderson, P., Le Roy, E., Charette, M., Moore, W., et al. (2023). Actinium and radium fluxes from the seabed in the northeast Pacific Basin. *Marine Chemistry*, *250*, 104180. https://doi.org/10.1016/j.marchem.2022.104180

Key, R. M., Guinasso, N. L., & Schink, D. R. (1979). Emanation of radon-222 from marine sediments. *Marine Chemistry*, *7*(3), 221–250. https://doi.org/10.1016/0304-4203(79)90041-0

Kipp, L. E., Charette, M. A., Moore, W. S., Henderson, P. B., & Rigor, I. G. (2018). Increased fluxes of shelf-derived materials to the central Arctic Ocean. *Science Advances*, *4*(1), eaao1302. https://doi.org/10.1126/sciadv.aao1302

Kipp, L. E., Sanial, V., Henderson, P. B., van Beek, P., Reyss, J.-L., Hammond, D. E., et al. (2018). Radium isotopes as tracers of hydrothermal inputs and neutrally buoyant plume dynamics in the deep ocean. *Marine Chemistry*, *201*, 51–65. https://doi.org/10.1016/j.marchem.2017.06.011

Koczy, F. F. (1958). Natural radium as a tracer in the. *Ocean*, *18*, 351–357.

Kröll, V. (1953). Vertical distribution of radium in deep-sea sediments. *Nature*, *171*(4356), 742. https://doi.org/10.1038/171742a0

Ku, T. L., Huh, C. A., & Chen, P. S. (1980). Meridional distribution of ^{226}Ra in the eastern Pacific along GEOSECS cruise tracks. *Earth and Planetary Science Letters*, *49*(2), 293–308. https://doi.org/10.1016/0012-821X(80)90073-4

Ku, T. L., Li, Y. H., Mathieu, G. G., & Wong, H. K. (1970). Radium in the Indian-Antarctic Ocean south of Australia. *Journal of Geophysical Research*, *75*(27), 5286–5292. https://doi.org/10.1029/JC075i027p05286

Ku, T.-L., & Lin, M.-C. (1976). ^{226}Ra distribution in the Antarctic Ocean. *Earth and Planetary Science Letters*, *32*(2), 236–248. https://doi.org/10.1016/0012-821X(76)90064-9

Ku, T.-L., & Luo, S. (1994). New appraisal of radium 226 as a large-scale oceanic mixing tracer. *Journal of Geophysical Research*, *99*(C5), 10255–10273. https://doi.org/10.1029/94JC00089

Kwon, E. Y., Kim, G., Primeau, F., Moore, W. S., Cho, H.-M., DeVries, T., et al. (2014). Global estimate of submarine groundwater discharge based on an observationally constrained radium isotope model. *Geophysical Research Letters*, *41*(23), 2014GL061574. https://doi.org/10.1002/2014GL061574

Lawrence, R. M., Shrikumar, A., Le Roy, E., Swift, J. H., Lam, P. J., Cutter, G., & Casciotti, K. L. (2022). Water mass analysis of the 2018 US GEOTRACES Pacific Meridional Transect (GP15). https://doi.org/10.1002/essoar.10510438.1

Lea, D., & Boyle, E. (1989). Barium content of benthic foraminifera controlled by bottom-water composition. *Nature*, *338*(6218), 751–753. https://doi.org/10.1038/338751a0

Lea, D. W., & Boyle, E. A. (1990). Foraminiferal reconstruction of barium distributions in water masses of the glacial oceans. *Paleoceanography*, *5*(5), 719–742. https://doi.org/10.1029/PA005i005p00719

Legeleux, F., & Reyss, J.-L. (1996). ^{228}Ra^{226}Ra activity ratio in oceanic settling particles: Implications regarding the use of barium as a proxy for paleoproductivity reconstruction. *Deep Sea Research Part I: Oceanographic Research Papers*, *43*(11), 1857–1863. https://doi.org/10.1016/S0967-0637(96)00086-6

Le Gland, G., Mémery, L., Aumont, O., & Resplandy, L. (2017). Improving the inverse modeling of a trace isotope: How precisely can radium-228 fluxes toward the ocean and submarine groundwater discharge be estimated? *Biogeosciences*, *14*(13), 3171–3189. https://doi.org/10.5194/bg-14-3171-2017

Le Roy, E., Sanial, V., Charette, M. A., van Beek, P., Lacan, F., Jacquet, S. H. M., et al. (2018). The ^{226}Ra–Ba relationship in the North Atlantic during GEOTRACES-GA01. *Biogeosciences*, *15*(9), 3027–3048. https://doi.org/10.5194/bg-15-3027-2018

Li, Y.-H., & Chan, L.-H. (1979). Desorption of Ba and ^{226}Ra from river-borne sediments in the Hudson estuary. *Earth and Planetary Science Letters*, *43*(3), 343–350. https://doi.org/10.1016/0012-821X(79)90089-X

Li, Y. H., Ku, T. L., Mathieu, G. G., & Wolgemuth, K. (1973). Barium in the Antarctic Ocean and implications regarding the marine geochemistry of Ba and226Ra. *Earth and Planetary Science Letters*, *19*(3), 352–358. https://doi.org/10.1016/0012-821X(73)90085-X

Light, T., Garcia, M., Prairie, J. C., Martínez-Ruiz, F., & Norris, R. (2023b). Water column barium sulfate dissolution and shielding by organic matter aggregates: Implications for the pelagic barite proxy. *Chemical Geology*, *636*, 121637. https://doi.org/10.1016/j.chemgeo.2023.121637

Light, T., Martínez-Ruiz, F., & Norris, R. (2023a). Marine barite morphology as an indicator of biogeochemical conditions within organic matter aggregates. *Geochimica et Cosmochimica Acta*, *358*, 38–48. https://doi.org/10.1016/j.gca.2023.08.012

Light, T., & Norris, R. (2021). Quantitative visual analysis of marine barite microcrystals: Insights into precipitation and dissolution dynamics. *Limnology & Oceanography*, *66*(10), 3619–3629. https://doi.org/10.1002/lno.11902

Lucas, H. F. (1957). Improved low-level alpha-scintillation counter for radon. *Review of Scientific Instruments*, *28*(9), 680–683. https://doi.org/10.1063/1.1715975

Lupton, J. (1998). Hydrothermal helium plumes in the Pacific Ocean. *Journal of Geophysical Research*, *103*(C8), 15853–15868. https://doi.org/10.1029/98JC00146

Mantyla, A. W., & Reid, J. L. (1983). Abyssal characteristics of the World Ocean waters. *Deep-Sea Research, Part A: Oceanographic Research Papers*, *30*(8), 805–833. https://doi.org/10.1016/0198-0149(83)90002-X

Martin, J.-M., & Meybeck, M. (1979). Elemental mass-balance of material carried by major world rivers. *Marine Chemistry*, *7*(3), 173–206. https://doi.org/10.1016/0304-4203(79)90039-2

Martinez-Ruiz, F., Paytan, A., Gonzalez-Muñoz, M. T., Jroundi, F., Abad, M. M., Lam, P. J., et al. (2019). Barite formation in the ocean: Origin of amorphous and crystalline precipitates. *Chemical Geology*, *511*, 441–451. https://doi.org/10.1016/j.chemgeo.2018.09.011

Mathieu, G. G., Wolgemuth, K., & Wolgemuth, K. (1973). Barium in the Antarctic Ocean and implication regarding the marine geochemsitry of Ba and ^{226}Ra. *Earth and Planetary Science Letters*, *19*(3), 352–358. https://doi.org/10.1016/0012-821x(73)90085-x

Matsumoto, K. (2007). Radiocarbon-based circulation age of the world oceans. *Journal of Geophysical Research*, *112*(C9), C09004. https://doi.org/10.1029/2007JC004095

Mayfield, K. K., Eisenhauer, A., Santiago Ramos, D. P., Higgins, J. A., Horner, T. J., Auro, M., et al. (2021). Groundwater discharge impacts marine isotope budgets of Li, Mg, Ca, Sr, and Ba. *Nature Communications*, *12*(1), 148. https://doi.org/10.1038/s41467-020-20248-3

McManus, J., Berelson, W. M., Hammond, D. E., & Klinkhammer, G. P. (1999). Barium cycling in the North Pacific: Implications for the utility of Ba as a paleoproductivity and paleoalkalinity proxy. *Paleoceanography*, *14*(1), 53–61. https://doi.org/10.1029/1998PA900007

Mete, Ö., Subhas, A., Kim, H., Dunlea, A., Whitmore, L., Shiller, A., et al. (2023). Barium in seawater: Dissolved distribution, relationship to silicon, and barite saturation state determined using machine learning. In *Earth system science data discussions* (pp. 1–42). https://doi.org/10.5194/essd-2023-67

Meybeck, M., & Ragu, A. (1997). Presenting the GEMS-GLORI, a compendium of world river discharge to the oceans. Retrieved from https://www.semanticscholar.org/paper/Presenting-the-GEMS-GLORI%2C-a-compendium-of-world-to-Meybeck-Ragu/171b8e1af28891cee5690925c5d8baf4b5c68c7f

Monnin, C., Jeandel, C., Cattaldo, T., & Dehairs, F. (1999). The marine barite saturation state of the world's oceans. *Marine Chemistry*, *65*(3), 253–261. https://doi.org/10.1016/S0304-4203(99)00016-X

Montes, I., Dewitte, B., Gutknecht, E., Paulmier, A., Dadou, I., Oschlies, A., & Garçon, V. (2014). High-resolution modeling of the Eastern Tropical Pacific oxygen minimum zone: Sensitivity to the tropical oceanic circulation. *Journal of Geophysical Research: Oceans*, *119*(8), 5515–5532. https://doi.org/10.1002/2014JC009858

Moore, W. S. (1976). Sampling ^{228}Ra in the deep ocean. *Deep-Sea Research and Oceanographic Abstracts*, *23*(7), 647–651. https://doi.org/10.1016/0011-7471(76)90007-3

Moore, W. S. (1996). Large groundwater inputs to coastal waters revealed by ^{226}Ra enrichments. *Nature*, *380*(6575), 612–614. https://doi.org/10.1038/380612a0

Moore, W. S. (1997). High fluxes of radium and barium from the mouth of the Ganges-Brahmaputra River during low river discharge suggest a large groundwater source. *Earth and Planetary Science Letters*, *150*(1), 141–150. https://doi.org/10.1016/S0012-821X(97)00083-6

Moore, W. S., Charette, M. A., Henderson, P. B., Hammond, D. E., Kemnitz, N., Le Roy, E., et al. (2024). Enriched regions of ^{228}Ra along the U.S. GEOTRACES Pacific meridional transect (GP15). *Journal of Geophysical Research: Oceans*, *129*(3), e2023JC020564. https://doi.org/10.1029/2023JC020564

Moore, W. S., & Dymond, J. (1991). Fluxes of ^{226}Ra and barium in the Pacific Ocean: The importance of boundary processes. *Earth and Planetary Science Letters*, *107*(1), 55–68. https://doi.org/10.1016/0012-821X(91)90043-H

Moore, W. S., Frankle, J. D., Benitez-Nelson, C. R., Früh-Green, G. L., & Lang, S. Q. (2021). Activities of ^{223}Ra and ^{226}Ra in fluids from the lost city hydrothermal field require short fluid residence times. *Journal of Geophysical Research: Oceans*, *126*(12), e2021JC017886. https://doi.org/10.1029/2021JC017886

Moore, W. S., & Shaw, T. J. (2008). Fluxes and behavior of radium isotopes, barium, and uranium in seven Southeastern US rivers and estuaries. *Marine Chemistry*, *108*(3–4), 236–254. https://doi.org/10.1016/j.marchem.2007.03.004

Neuholz, R., Schnetger, B., Kleint, C., Koschinsky, A., Lettmann, K., Sander, S., et al. (2020). Near-field hydrothermal plume dynamics at Brothers Volcano (Kermadec Arc): A short-lived radium isotope study. *Chemical Geology*, *533*, 119379. https://doi.org/10.1016/j.chemgeo.2019.119379

Nielsen, S. G., Rehkämper, M., Teagle, D. A. H., Butterfield, D. A., Alt, J. C., & Halliday, A. N. (2006). Hydrothermal fluid fluxes calculated from the isotopic mass balance of thallium in the ocean crust. *Earth and Planetary Science Letters*, *251*(1), 120–133. https://doi.org/10.1016/j.epsl.2006.09.002

Nürnberg, C. C., Bohrmann, G., Schlüter, M., & Frank, M. (1997). Barium accumulation in the Atlantic sector of the Southern Ocean: Results from 190,000-year records. *Paleoceanography*, *12*(4), 594–603. https://doi.org/10.1029/97PA01130

Orsi, A. H., Johnson, G. C., & Bullister, J. L. (1999). Circulation, mixing, and production of Antarctic Bottom Water. *Progress in Oceanography*, *43*(1), 55–109. https://doi.org/10.1016/S0079-6611(99)00004-X

Östlund, H. G., Craig, H. C., Broecker, W. S., & Spencer, D. W., & GEOSECS. (1987). Shorebased measurements during the GEOSECS Pacific expedition. https://doi.org/10.1594/PANGAEA.743238

Paytan, A., & Kastner, M. (1996). Benthic Ba fluxes in the central Equatorial Pacific, implications for the oceanic Ba cycle. *Earth and Planetary Science Letters*, *142*(3), 439–450. https://doi.org/10.1016/0012-821X(96)00120-3

Paytan, A., Moore, W. S., & Kastner, M. (1996). Sedimentation rate as determined by ^{226}Ra activity in marine barite. *Geochimica et Cosmochimica Acta*, *60*(22), 4313–4319. https://doi.org/10.1016/S0016-7037(96)00267-0

Peterson, R. N., Burnett, W. C., Dimova, N., & Santos, I. R. (2009). Comparison of measurement methods for radium-226 on manganese-fiber. *Limnology and Oceanography: Methods*, *7*(2), 196–205. https://doi.org/10.4319/lom.2009.7.196

Rahaman, W., & Singh, S. K. (2023). Behaviour of barium in the tropical estuaries: Implications to its marine budgets and paleo-oceanographic applications. *Marine Chemistry*, *254*, 104278. https://doi.org/10.1016/j.marchem.2023.104278

Rahman, S., Shiller, A. M., Anderson, R. F., Charette, M. A., Hayes, C. T., Gilbert, M., et al. (2022). Dissolved and particulate barium distributions along the US GEOTRACES North Atlantic and East Pacific zonal transects (GA03 and GP16): Global implications for the marine barium cycle. *Global Biogeochemical Cycles*, *36*(6), e2022GB007330. https://doi.org/10.1029/2022GB007330

Rommets, J. W., Stoll, M. H. C., de Koster, R. X., de Bruin, T. F., de Baar, H. J. W., Bathmann, U., & Smetacek, V. (1997). *Database of the JGOFS expedition ANT X/6 aboard R.V. Polarstern, Smetacek, Victor; de Baar, Hein JW; Bathmann, Ulrich; Lochte, Karin; Rutgers van der Loeff, Michiel M (1997): Ecology and biogeochemistry of the Antarctic circumpolar current during austral spring: Southern Ocean JGOFS Cruise ANT X/6 of R.V. Polarstern. D, Bremerhaven*. PANGAEA.

Rushdi, A. I., McManus, J., & Collier, R. W. (2000). Marine barite and celestite saturation in seawater. *Marine Chemistry*, *69*(1), 19–31. https://doi.org/10.1016/S0304-4203(99)00089-4

Rutgers van der Loeff, M., Kipp, L., Charette, M. A., Moore, W. S., Black, E., Stimac, I., et al. (2018). Radium isotopes across the Arctic Ocean show time scales of water mass ventilation and increasing shelf inputs. *Journal of Geophysical Research: Oceans*, *123*(7), 4853–4873. https://doi.org/10.1029/2018JC013888

Sanial, V., Kipp, L. E., Henderson, P. B., van Beek, P., Reyss, J.-L., Hammond, D. E., et al. (2017). Radium-228 as a tracer of dissolved trace element inputs from the Peruvian continental margin. *Marine Chemistry*, *201*, 20–34. https://doi.org/10.1016/j.marchem.2017.05.008

Sarmiento, J. L., Gruber, N., Brzezinski, M. A., & Dunne, J. P. (2004). High-latitude controls of thermocline nutrients and low latitude biological productivity. *Nature*, *427*(6969), 56–60. https://doi.org/10.1038/nature02127

Shannon, L. V., & Cherry, R. D. (1971). Radium-226 in marine phytoplankton. *Earth and Planetary Science Letters*, *11*(1), 339–343. https://doi.org/10.1016/0012-821X(71)90189-0

Shaw, T. J., Moore, W. S., Kloepfer, J., & Sochaski, M. A. (1998). The flux of barium to the coastal waters of the southeastern USA: The importance of submarine groundwater discharge. *Geochimica et Cosmochimica Acta*, *62*(18), 3047–3054. https://doi.org/10.1016/S0016-7037(98)00218-X

Shiller, A. M. (2021a). Dissolved Barium (Ba) from R/V Thomas G. Thompson cruise TN303 (GP16) in the Eastern Tropical Pacific in 2013 (U.S. GEOTRACES EPZT project) (version 2) [Dataset]. *BCO-DMO*. https://doi.org/10.26008/1912/BCO-DMO.648753.2

Shiller, A. M. (2021b). Dissolved concentrations of Ba, Cd, Cu, Ga, Mn, Nd, Ni, and Pb from Leg 1 (Seattle, WA to Hilo, HI) of the US GEOTRACES Pacific Meridional Transect (PMT) cruise (GP15, RR1814) on R/V Roger Revelle from September to October 2018 (Version 3) [Dataset]. *Biological and Chemical Oceanography Data Management Office (BCO-DMO)*. https://doi.org/10.26008/1912/BCO-DMO.835589.3

Shiller, A. M. (2021c). Dissolved concentrations of Ba, Cd, Cu, Ga, Mn, Nd, Ni, and Pb from Leg 2 (Hilo, HI to Papeete, French Polynesia) of the US GEOTRACES Pacific Meridional Transect (PMT) cruise (GP15, RR1815) on R/V Roger Revelle from Oct-Nov 2018 (Version 2) [Dataset]. *Biological and Chemical Oceanography Data Management Office (BCO-DMO)*. https://doi.org/10.26008/1912/BCO-DMO.836121.2

Shrikumar, A., Lawrence, R., & Casciotti, K. L. (2022). PYOMPA technical note (preprint). *Oceanography*. https://doi.org/10.1002/essoar.10507053.4

Silva, N., Rojas, N., & Fedele, A. (2009). Water masses in the Humboldt Current System: Properties, distribution, and the nitrate deficit as a chemical water mass tracer for Equatorial Subsurface Water off Chile. *Deep Sea Research Part II: Topical Studies in Oceanography*, *56*(16), 1004–1020. https://doi.org/10.1016/j.dsr2.2008.12.013

Steiner, Z., Antler, G., Berelson, W. M., Crockford, P. W., Dunlea, A. G., Hou, Y., et al. (2023). Trace element geochemistry in North Pacific red clay sediment porewaters and implications for water-column studies. *Global Biogeochemical Cycles*, *37*(11), e2023GB007844. https://doi.org/10.1029/2023GB007844

Sternberg, E., Tang, D., Ho, T.-Y., Jeandel, C., & Morel, F. M. M. (2005). Barium uptake and adsorption in diatoms. *Geochimica et Cosmochimica Acta*, *69*(11), 2745–2752. https://doi.org/10.1016/j.gca.2004.11.026

Stramma, L., Johnson, G. C., Firing, E., & Schmidtko, S. (2010). Eastern Pacific oxygen minimum zones: Supply paths and multidecadal changes. *Journal of Geophysical Research*, *115*(C9), C09011. https://doi.org/10.1029/2009JC005976

Stroobants, N., Dehairs, F., Goeyens, L., Vanderheijden, N., & Van Grieken, R. (1991). Barite formation in the Southern Ocean water column. *Marine Chemistry*, *35*(1), 411–421. https://doi.org/10.1016/S0304-4203(09)90033-0

Strub, P. T., Shillington, F. A., James, C., & Weeks, S. J. (1998). Satellite comparison of the seasonal circulation in the Benguela and California current systems. *African Journal of Marine Science*, *19*(1), 99–112. https://doi.org/10.2989/025776198784126836

Subhas, A. V., Pavia, F. J., Dong, S., & Lam, P. J. (2023). Global trends in the distribution of biogenic minerals in the ocean. *Journal of Geophysical Research: Oceans*, *128*(2), e2022JC019470. https://doi.org/10.1029/2022JC019470

Sverdrup, Johnson, & Fleming (1942). The oceans their physics, chemistry, and general biology. Retrieved from https://publishing.cdlib.org/ucpressebooks/view?docId=kt167nb66r&chunk.id=0&doc.view=print

Szabo, B. J. (1967). Radium content in plankton and sea water in the Bahamas. *Geochimica et Cosmochimica Acta*, *31*(8), 1321–1331. https://doi.org/10.1016/S0016-7037(67)80018-8

Talley, L. (2013). Closure of the global overturning circulation through the Indian, Pacific, and southern oceans: Schematics and Transports. *Oceanography*, *26*(1), 80–97. https://doi.org/10.5670/oceanog.2013.07

Talley, L. D. (1997). North Pacific intermediate water transports in the mixed water region. *Journal of Physical Oceanography*, *27*(8), 1795–1803. https://doi.org/10.1175/1520-0485(1997)027<1795:NPIWTI>2.0.CO;2

Talley, L. D., Pickard, G. L., Emery, W. J., & Swift, J. H. (2011a). Chapter 10 - Pacific Ocean. In *Descriptive physical oceanography* (6th ed., pp. 303–362). Academic Press. https://doi.org/10.1016/B978-0-7506-4552-2.10010-1

Talley, L. D., Pickard, G. L., Emery, W. J., & Swift, J. H. (2011b). Chapter S10 - Pacific Ocean: Supplementary materials. In *Descriptive physical oceanography* (6th ed., pp. 1–31). Academic Press. https://doi.org/10.1016/B978-0-7506-4552-2.10022-8

Tomczak, M., & Liefrink, S. (2005). Interannual variations of water mass volumes in the Southern Ocean. *Journal of Atmospheric and Ocean Science*, *10*(1), 31–42. https://doi.org/10.1080/17417530500062838

Torres, M. E., Bohrmann, G., & Suess, E. (1996). Authigenic barites and fluxes of barium associated with fluid seeps in the Peru subduction zone. *Earth and Planetary Science Letters*, *144*(3), 469–481. https://doi.org/10.1016/S0012-821X(96)00163-X

Tréguer, P. J. (2014). The Southern Ocean silica cycle. *Comptes Rendus Geoscience*, *346*(11–12), 279–286. https://doi.org/10.1016/j.crte.2014.07.003

Tsuchiya, M., & Talley, L. D. (1998). A Pacific hydrographic section at 88°W: Water-property distribution. *Journal of Geophysical Research*, *103*(C6), 12899–12918. https://doi.org/10.1029/97JC03415

van Beek, P., François, R., Conte, M., Reyss, J.-L., Souhaut, M., & Charette, M. (2007). $^{228}Ra/^{226}Ra$ and $^{226}Ra/Ba$ ratios to track barite formation and transport in the water column. *Geochimica et Cosmochimica Acta*, *71*(1), 71–86. https://doi.org/10.1016/j.gca.2006.07.041

van Beek, P., François, R., Honda, M., Charette, M. A., Reyss, J.-L., Ganeshram, R., et al. (2022). Fractionation of ^{226}Ra and Ba in the Upper North Pacific Ocean. *Frontiers in Marine Science*, *9*. https://doi.org/10.3389/fmars.2022.859117

van Beek, P., Souhaut, M., & Reyss, J.-L. (2010). Measuring the radium quartet (^{228}Ra, ^{226}Ra, ^{224}Ra, ^{223}Ra) in seawater samples using gamma spectrometry. *Journal of Environmental Radioactivity*, *101*(7), 521–529. https://doi.org/10.1016/j.jenvrad.2009.12.002

von Damn, K. L., Edmond, J. M., Grant, C. I., Measures, C. I., Walden, B., & Weiss, R. F. (1985). Chemistry of submarine hydrothermal solutions at 21°N, East Pacific Rise. *Geochimica et Cosmochimica Acta*, *49*(11), 2197–2220. https://doi.org/10.1016/0016-7037(85)90222-4

Wijffels, S. E., Toole, J. M., & Davis, R. (2001). Revisiting the South Pacific subtropical circulation: A synthesis of world ocean circulation experiment observations along 32°S. *Journal of Geophysical Research*, *106*(C9), 19481–19513. https://doi.org/10.1029/1999JC000118

Wolgemuth, K., & Broecker, W. S. (1970). Barium in sea water. *Earth and Planetary Science Letters*, *8*(5), 372–378. https://doi.org/10.1016/0012-821X(70)90110-X

Xu, B., Li, S., Burnett, W. C., Zhao, S., Santos, I. R., Lian, E., et al. (2022). Radium-226 in the global ocean as a tracer of thermohaline circulation: Synthesizing half a century of observations. *Earth-Science Reviews*, *226*, 103956. https://doi.org/10.1016/j.earscirev.2022.103956